

# Non-double-couple mechanisms of microearthquakes induced during the 2000 injection experiment at the KTB site, Germany: A result of tensile faulting or anisotropy of a rock?

Václav Vavryčuk<sup>a,\*</sup>, Marco Bohnhoff<sup>b</sup>, Zuzana Jechumtálová<sup>a</sup>, Petr Kolář<sup>a</sup>, Jan Šílený<sup>a</sup>

<sup>a</sup> Geophysical Institute, Academy of Sciences of the Czech Republic, Boční II/1401, Praha 4, 141 31, Czech Republic

<sup>b</sup> GeoForschungsZentrum Potsdam, Telegrafenberg, D-14473, Potsdam, Germany

Received 14 May 2007; accepted 24 August 2007

Available online 26 February 2008

## Abstract

Moment tensors of microearthquakes induced during the 2000 injection experiment at the KTB deep drilling borehole at a depth level of 5.4 km are studied. A family of 37 most reliable moment tensors contains significant non-double-couple (non-DC) components. The DC is on average 60% and the non-DC is 40%. Fault plane solutions computed from the DC part show preferred strike-slip mechanisms with small normal or reverse components. A predominant azimuth of *P* and *T* axes is in the range of N320°–340°E and of N230°–250°E, respectively. The non-DC components contain both the isotropic (ISO) and compensated linear vector dipole (CLVD) components. The mean value of ISO is 1.5%, the mean value of CLVD is –5.7%. The predominantly negative CLVD components are inconsistent with the concept of the non-DC mechanisms as a result of tensile faulting due to fluid injection into the rock. The main origin of the non-DC components is probably anisotropy in the focal area. The other origins are errors produced by mismodelling of the medium when calculating the Green functions, and numerical errors produced by noise and limitations of input data. Adopting four alternative models of anisotropy obtained by other seismic measurements at the KTB, we have employed the non-DC components for estimating an optimum orientation of anisotropy in the focal area. The optimum orientation of the symmetry plane of anisotropy is nearly vertical with a strike of N335°–340°E. This strike coincides well with the strike of 330° typical for many major lithological units and faults and with the orientation of the transversely isotropic model inferred by other authors. After removing the anisotropy effects from the moment tensors by calculating the source tensors, the distribution of ISO is significantly narrowed. This indicates predominantly shear, but not tensile faulting.

© 2008 Elsevier B.V. All rights reserved.

**Keywords:** Anisotropy; Fluid injection; Focal mechanism; Tensile faulting

## 1. Introduction

A 60-day long-term fluid injection experiment was performed at the German KTB superdeep drilling hole in 2000 (Baisch et al., 2002). The KTB site is located in southeast Germany at the western margin of the Bohemian Massif, at the contact zone of the Saxothuringian with the Moldanubian (Wagner et al., 1997). About 4000 m<sup>3</sup> of water were injected into the well head to induce seismicity near the open-hole section at a

depth of 9.1 km. The entire borehole was pressurized and the well head pressure gradually increased during the experiment from 20 to 30 MPa. The injection was interrupted by several sharp pressure drops during shut-in phases. The injected fluid induced seismicity not only at the target depth but also at shallower depths because of leaks in the borehole casing. The seismicity was monitored by a surface network of 40 three-component seismic stations and by one downhole three-component sensor at a depth of 3.8 km, situated at the nearby pilot hole (see Fig. 1). A total of 2799 induced microearthquakes were detected at the downhole sensor, and 237 of them were located using records at the surface stations (Baisch et al.,

\* Corresponding author.

E-mail address: [vv@ig.cas.cz](mailto:vv@ig.cas.cz) (V. Vavryčuk).

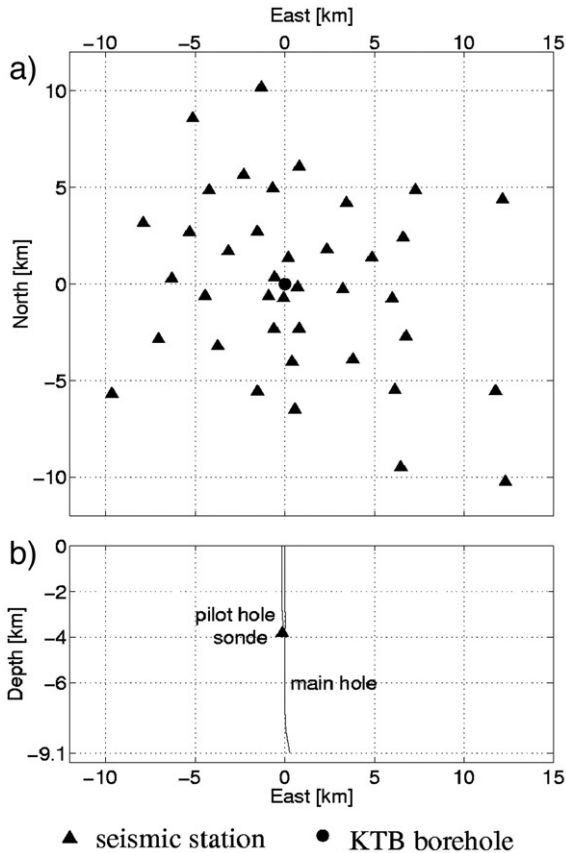


Fig. 1. The temporary seismic network operating during the 2000 injection experiment (after Bohnhoff et al., 2004). (a) Map view of the network. The position of the KTB main hole is indicated by the dot. (b) Cross view of the main and pilot holes (view from the south).

2002). The event locations revealed that the hypocenter distribution is complex and displays strong spatial and temporal clustering. Fault plane solutions have been calculated for 125 events by Bohnhoff et al. (2004). The fault plane solutions show preferred strike-slip mechanisms with a predominant azimuth in the range of N155°–175°E for *P* axes and of N50°–80°E for *T* axes. The mechanisms are in good agreement with the stress field at the KTB (Brudy et al., 1997) and in western and central Europe (Müller et al., 1992).

In this paper, we continue studying the seismicity induced during the 2000 injection experiment and try to estimate moment tensors of selected events. Evaluating the complete moment tensors we can get more detailed information on the geometry of fractures, the fracture process and on the properties of fractured rock (Sipkin, 1986; Frohlich, 1994; Julian et al., 1997, 1998; Müller et al., 1998; Foulger et al., 2004). A careful evaluation of the moment tensors and their DC and non-DC components of events induced during the injection can address several intriguing topics not yet well understood, such as the impact of the fluid injection on the type of faulting and of anisotropy in the focal area on focal mechanisms.

As regards the relation between the fluid injection and the type of faulting, we know that fluid injected into a rock under sufficiently high pressure can cause hydraulic fracturing or opening of existing faults (Vavryčuk, 2002), which is associated

with an occurrence of combined shear and tensile faulting. Since moment tensors are very sensitive to the presence of a tensile component in faulting, they can be used to vindicate it. Vavryčuk (2001) showed that even small deviations from shear faulting can be detected by evaluating the moment tensors. For example, a 10° declination of slip from the fault results in lowering the percentage of the DC component in the moment tensors from 100% to 70%, and a 20° declination causes a drop of the DC from 100% to a mere 50% (Vavryčuk, 2001). Such drops of the DC component in moment tensors should be easily detected in well-determined moment tensors.

In evaluating moment tensors we can also study how significant anisotropy in the focal area is. Vavryčuk (2005, 2006b) has shown that moment tensors are affected by anisotropy of the rock surrounding the fault. While shear faulting on planar faults in an isotropic medium is represented by a pure DC mechanism, shear faulting on planar faults in an anisotropic medium is represented by a general mechanism with DC as well as non-DC components. In anisotropic rocks present in the Earth’s crust, the non-DC components can attain values up to 40–50%. This percentage depends on strength and symmetry of anisotropy and on the orientation of faulting. If we evaluate a set of accurate moment tensors of events that occurred in a homogeneous anisotropic focal area on differently oriented faults, we can invert them for anisotropy (Vavryčuk, 2004, 2006a).

## 2. Data

The events under study form a subset of 125 events used for calculating focal mechanisms by Bohnhoff et al. (2004). The 125 events consist of 102 events that occurred at a depth level of 5.4 km, and of 23 events that occurred at a depth level of 9 km. To avoid mixing mechanisms of events from different depths and to optimize a focal coverage by rays, we focused at the depth level of 5.4 km. this depth provides excellent conditions for determining confident moment tensors (see Fig. 2). From the

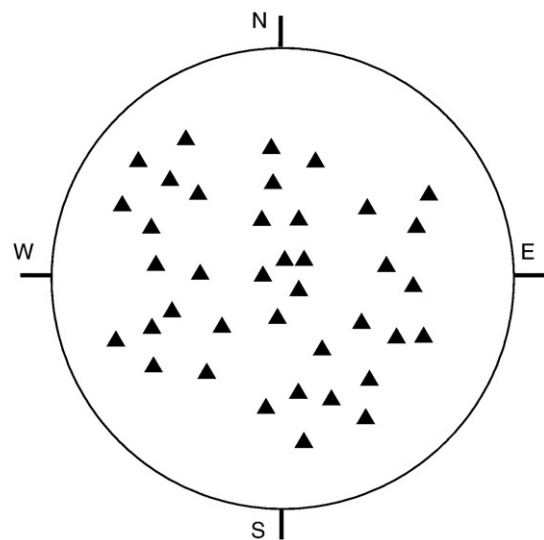


Fig. 2. The focal sphere coverage for temporary seismic stations. The source is located at depth of 5400 m. Lower-hemisphere equal area projection is used.

Table 1a  
Locations and moment tensors: reliable events

No.	Event identification	$M_L$	$N^S$	$N$ [m]	$E$ [m]	$Z$ [m]	$M_{11}$	$M_{12}$	$M_{13}$	$M_{22}$	$M_{23}$	$M_{33}$
1	235.008	0.38	21	-90	80	5310	-0.90	1.54	0.70	1.10	-0.40	0.82
2	235.025	-0.34	11	-80	-150	5320	-1.00	1.08	-0.34	1.42	-0.04	-0.06
3	236.041	1.10	27	-130	-40	5340	-1.00	0.68	-0.96	0.64	0.24	-0.24
4	237.024	-0.05	7	-10	30	5130	-0.34	1.52	-0.94	1.04	0.16	0.20
5	252.199	0.47	30	-90	-10	5310	-0.88	1.24	-0.84	0.68	-0.42	0.28
6	255.002	-0.11	23	-120	50	5430	-0.90	1.54	-0.12	0.28	-0.12	-0.02
7	258.009	0.06	7	70	-130	5410	0.26	1.52	-0.72	1.30	0.18	0.48
8	258.010	0.07	13	-110	-100	5330	-0.88	1.04	-0.90	0.46	1.02	0.40
9	259.065	0.22	9	-120	-40	5270	1.10	1.54	-0.66	1.32	0.04	0.20
10	261.016	0.02	13	-120	-30	5340	-0.78	1.26	-0.32	0.90	-0.02	0.06
11	262.070	-0.55	32	-100	-40	5370	-0.96	1.52	-0.80	0.18	-0.38	0.44
12	264.012	-0.69	9	-100	-40	5300	1.32	1.46	-0.88	1.42	0.24	0.14
13	264.084	-0.01	7	-100	-100	5370	-0.80	1.00	0.26	-0.20	0.12	-0.96
14	266.058	0.55	31	10	-100	5340	-0.84	1.34	-0.46	1.06	0.52	-0.22
15	267.134	0.14	20	220	10	5330	-0.42	0.82	-0.38	1.44	0.14	-0.50
16	268.172	0.18	25	-10	-90	5450	1.20	0.70	1.08	1.32	0.42	-0.72
17	269.055	-0.01	20	-50	-70	5330	-0.90	1.46	-0.76	1.48	0.20	-0.22
18	271.280	0.15	29	-360	170	5200	-1.00	1.08	-0.42	0.64	0.66	0.02
19	275.016	0.92	31	-100	40	5370	-0.96	1.48	-0.80	0.92	0.52	-0.40
20	275.026	0.21	21	-40	20	5340	-1.00	1.18	-0.56	0.22	-0.90	0.02
21	275.027	0.87	33	-160	20	5330	-0.98	1.54	-0.72	0.08	-0.08	0.30
22	275.094	-0.13	18	-290	0	5470	-1.00	1.22	0.46	-0.78	0.08	0.06
23	276.086	0.05	13	-60	-150	5290	1.06	1.30	1.22	1.38	-0.50	0.04
24	278.066	0.06	9	-110	60	5480	-0.64	1.52	1.36	0.32	-0.16	0.38
25	279.073	0.17	21	-10	-40	5350	-0.86	1.08	-1.00	1.12	-0.94	0.30
26	279.110	-0.19	13	120	-120	5200	0.20	1.40	-0.66	-1.00	-0.72	-0.02
27	280.054	0.35	20	-220	40	5350	-0.04	1.34	-0.32	-0.22	-0.10	-0.98
28	281.018	0.20	30	-80	-80	5330	-0.94	1.44	-0.66	1.08	0.00	-0.54
29	281.047	0.72	31	-30	-10	5360	-0.72	1.52	-0.66	0.74	-0.26	0.10
30	282.012	-0.05	17	-90	10	5360	-0.22	1.54	-0.44	0.74	-0.16	-0.18
31	283.005	-0.13	8	0	-330	5200	0.16	1.48	0.70	1.02	0.14	-0.56
32	285.056	-0.26	16	-270	50	5580	-0.98	-0.14	-0.78	1.40	-0.72	-0.04
33	286.001	0.23	20	-170	160	5210	-1.00	1.20	-0.34	1.50	-0.14	0.36
34	288.030	-0.11	21	-230	50	5570	-0.92	1.32	-0.26	-0.92	-0.92	0.24
35	290.048	1.02	28	-140	-10	5300	-0.98	1.46	-0.64	0.44	0.90	0.38
36	291.059	-0.07	11	-150	170	5250	-0.86	1.10	-0.98	1.46	-0.06	0.76
37	297.016	0.40	10	-150	-200	5640	-0.94	1.52	0.06	-0.40	-0.08	0.28

$M_L$  is the body wave local magnitude,  $N^S$  is the number of surface stations, which detected the event,  $N$ ,  $E$ ,  $Z$  are coordinates of the hypocenter, and  $M_{11}$ ,  $M_{22}$ ,  $M_{33}$ ,  $M_{12}$ ,  $M_{13}$  and  $M_{23}$  are the components of moment tensor  $\mathbf{M}$  in relative values. The moment tensors are in the following coordinate system  $x_1=N$ ,  $x_2=E$ , and  $x_3=Z$  (downwards). The locations of events were adopted from Baisch et al. (2002).

Table 1b  
Locations and moment tensors: unreliable events

No.	Event identification	$M_L$	$N^S$	$N$ [m]	$E$ [m]	$Z$ [m]	$M_{11}$	$M_{12}$	$M_{13}$	$M_{22}$	$M_{23}$	$M_{33}$
38	237.040	0.45	8	-40	70	5170	1.14	1.28	-0.38	0.20	1.36	0.48
39	261.288	-0.66	11	-80	-190	5350	0.56	1.42	-0.20	0.92	0.32	-0.64
40	268.135	-0.77	4	-70	-100	5280	-0.74	0.08	-0.18	-0.64	0.54	-0.98
41	271.262	-0.60	6	-180	70	5280	0.26	0.48	-0.76	1.54	-0.58	-0.86
42	273.018	0.81	9	-100	-110	5330	0.76	1.18	-0.90	0.14	1.06	-0.82
43	274.176	-0.11	13	140	-270	5210	0.42	1.28	-1.00	1.36	1.34	0.24
44	275.097	-0.29	5	-210	-10	5270	0.14	0.30	-0.94	-0.02	-1.00	-0.76
45	281.058	0.05	5	-320	-150	5270	-1.00	1.50	0.52	1.54	-0.98	0.48
46	282.024	0.00	8	-150	-20	5150	-0.96	1.22	-0.92	1.46	0.14	0.16
47	283.032	-0.18	10	70	-180	5190	0.30	1.54	0.14	-0.58	1.08	-0.06
48	284.006	-0.12	9	100	-240	5180	-0.04	-0.44	1.46	1.28	1.16	0.98
49	286.040	-0.12	6	-120	-160	5170	1.50	1.54	0.20	-0.58	-0.54	-0.62
50	288.081	0.23	13	-90	-10	5280	-0.98	-0.36	-0.14	0.78	-0.90	0.14
51	294.023	0.82	16	-230	-200	5640	-0.98	1.36	-0.44	0.76	-0.56	-0.10
52	299.027	-0.11	9	-410	0	5540	1.52	-0.02	-0.02	-0.64	0.74	1.52

For the meaning of quantities, see the legend of Table 1a.

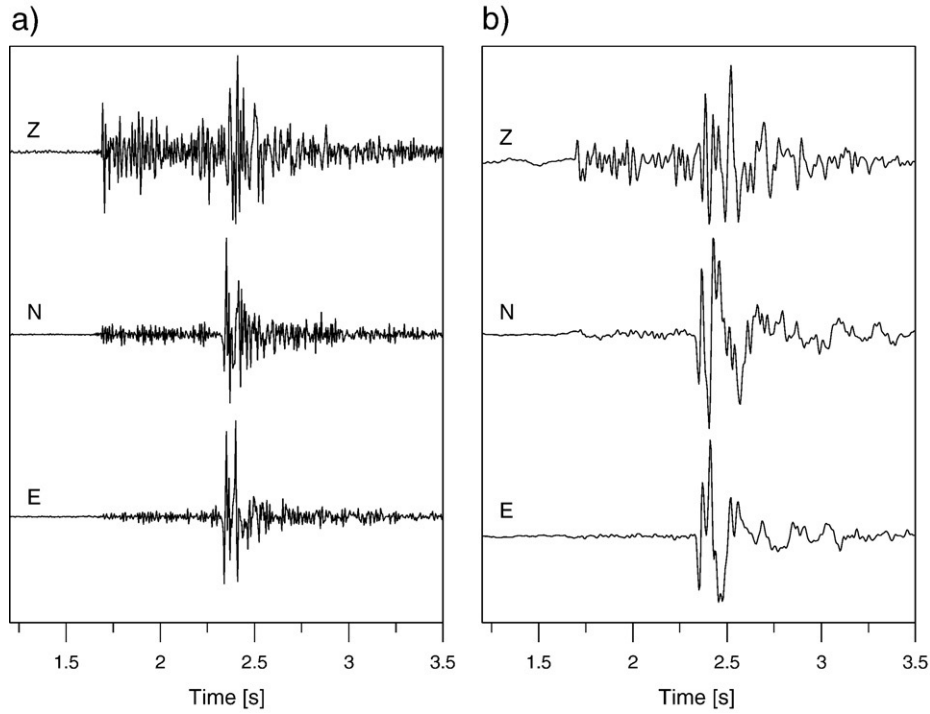


Fig. 3. A waveform of event 252.199 (see Table 1a) recorded at station no. 303. (a) Original data, (b) filtered and integrated data.

102 microearthquakes of Bohnhoff et al. (2004) that occurred at the target depth, we selected 52 microearthquakes having the best signal-to-noise ratio and being recorded at least at 4 surface stations (the most of events, however, were recorded at 15 or more surface stations, see Tables 1a and 1b). The selection of

the best recorded events was necessary to meet demands of the moment tensor inversion on the amount and quality of data.

The surface stations were equipped with PDAS-100 data logger and with three-component Mark L4-3c seismometers. The recording was continuous at a 200 Hz sampling rate. The

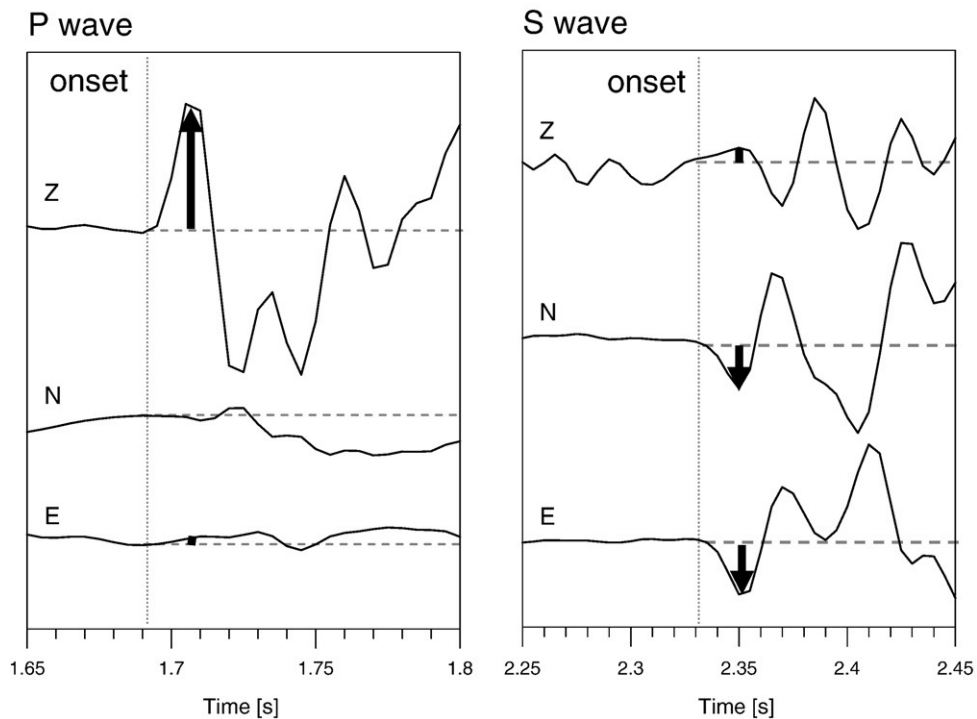


Fig. 4. Detailed waveforms of P and S phases of the event from Fig. 3. The arrows show P and S amplitudes used in the moment tensors inversion.

recorded velocigrams were filtered by a bandpass Butterworth filter of the 4th order extracting signal frequencies between 2.5–40 Hz with enhanced signal-to-noise ratio. The velocigrams were further integrated to obtain displacement records (see Fig. 3). From these records, particle motions of  $P$  and  $S$  waves were plotted and the first maximum  $P$ - and  $S$ -wave amplitudes were interactively picked (see Fig. 4).

### 3. Moment tensor inversion

#### 3.1. Procedure

The amplitude ratios of  $SH/P$ ,  $SV/P$  and  $SV/SH$  were computed from the  $P$  and  $S$  amplitudes picked from particle motions. The ratios together with polarities can be inverted either in a linear scheme (Julian and Foulger, 1996) or as a non-linear problem. We chose the latter way and used the inversion scheme of Jechumtálová and Šílený (2005) for inversion of the ratios and polarities of  $P$  waves to retrieve the complete moment tensor. The cost function was constructed as the sum of absolute values of differences of the logarithms of the observed and

synthetic amplitude ratios. The logarithms of amplitude ratios were used because they appeared to be more stable than if simple ratios were used. No constraint on the moment tensors (e.g., the zero-trace condition) was imposed in the inversion, hence the inversion was able to yield the full moment tensors with unconstrained DC and non-DC components. Inversion of amplitude ratios is more laborious than from amplitudes, but it is less vulnerable to erroneous modelling of the Earth's crust and to inaccuracies in the calibration of instruments. However, it yields only relative but not absolute values of the moment tensors.

#### 3.2. Model of the medium

The model of the medium and event locations, required to compute the synthetic amplitude ratios, were adopted from Baisch et al. (2002): a homogeneous isotropic halfspace with velocities  $v_p=6.08$  km/s,  $v_s=3.51$  km/s. The density of the medium is  $2800$  kg/m<sup>3</sup>.

Using a simple homogeneous isotropic model is supported by the fact that: (1) the crust at the KTB site is formed by crystalline rocks with a small velocity contrast amongst them,

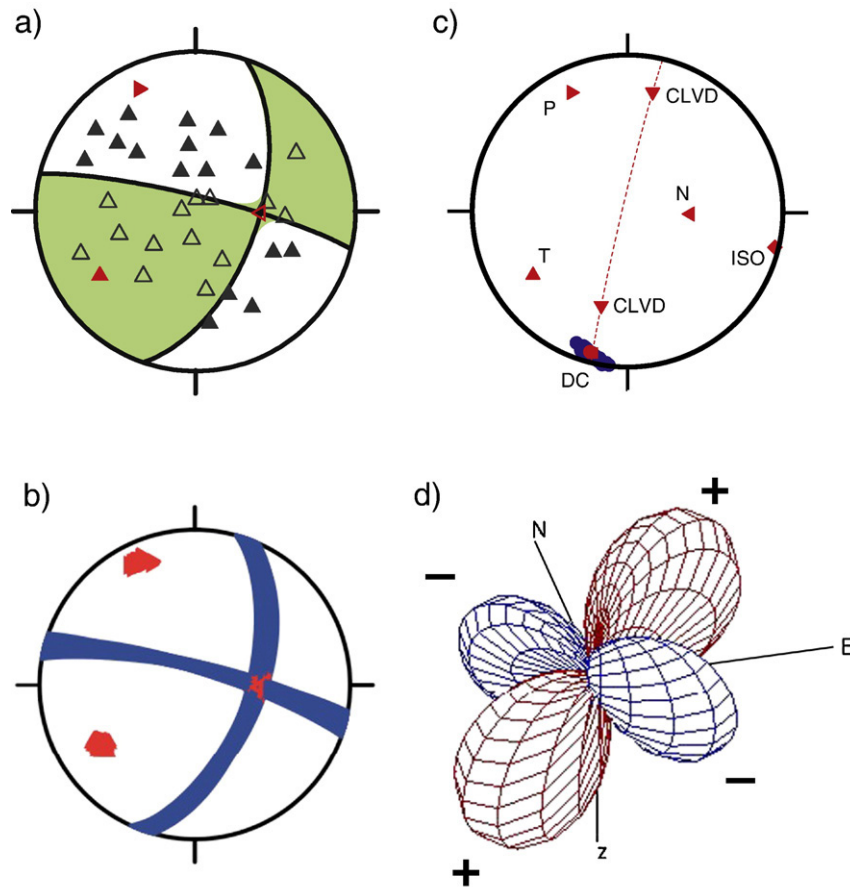


Fig. 5. An example of a reliably determined mechanism (event 252.199 in Table 1a). The figure shows: (a) the optimum fault-plane solution (the nodal lines of the DC part), (b) the distribution of the  $P$ ,  $N$  and  $T$  axes and of nodal lines obtained by the inversion of 100 realizations of noisy data, (c) the distribution of 100 solutions (blue dots) and the optimum solution (red dot) in the Riedesel–Jordan projection (Riedesel and Jordan, 1989), and (d) the  $P$ -wave radiation function for the optimum solution. The green area in plot (a) marks the zone of compressions corresponding to the complete moment tensor. The moment tensor principal axes are marked by red triangles: pointing up — tensional ( $T$ ) axis, pointing left — null ( $N$ ) axis, pointing right — pressure ( $P$ ) axis. The solid/open triangles mark stations on the focal sphere with the  $P$ -wave dilatation/compression. Clustering of  $P$ ,  $N$  and  $T$  axes and of nodal lines in plot (b) and clustering of solutions (blue dots) in plot (c) testifies the stability of the solution.  $E$ ,  $N$  and  $Z$  in plot (d) denote North, East and the vertical axis. The plus and minus signs define the polarity of the radiated  $P$  wave amplitude.

(2) the focal sphere displays an excellent and almost spatially uniform ray coverage, which should suppress disturbances caused by inhomogeneity or anisotropy, and (3) we are primarily not interested in characteristics of individual events, but in characteristics of the whole family of events. Obviously, the statistical properties of the moment tensors determined from various station configurations should be significantly less vulnerable to mismodelling of the medium than the moment tensors of individual events.

3.3. Sensitivity to random errors

The stability of the moment tensors retrieved was tested by observing the distributions of 100 solutions obtained by inverting the data contaminated by artificial random noise with the maximum amplitude reaching 5% of the top value in each channel. In this way, the distribution of the principal axes of moment tensors was obtained providing information on the stability of the orientation of their DC components. In addition, the bundles of nodal lines are plotted to display the stability of the fault plane solution. As an example of a reliably determined DC mechanism, event 252.199 is presented in Fig. 5: the principal axes of the moment tensors from the multiple processing of noisy data are close together, which indicates that the orientation of the mechanism is well constrained.

The reliability of the solution is manifested also by the tight clustering of nodal lines. Fig. 6 shows event 282.024 as an example of an unreliably determined mechanism. The orientation of the mechanism is poorly determined: the principal axes are scattered widely, and the zones of *T* and *N* axes are mixed together.

In analyzing the stability of the 52 inverted moment tensors, we selected 37 well-determined moment tensors for the purpose of our study (see Table 1a). The other 15 moment tensors were classified as unreliable and rejected from further analyses (see Table 1b). The reliable moment tensors were selected as follows: first, the sum of standard deviations of the DC and non-DC components  $\sigma^{\text{SUM}}$  was less than or equal to 50% (see Tables 2a and 2b). Second, the moment tensors displayed well-defined clustering of nodal lines in multiple inversions of data contaminated by noise. Third, the clusters of *P*, *N* and *T* axes were isolated and did not overlap (see Fig. 7). The unreliable moment tensors displayed remarkable ambiguities in focal mechanisms and the clusters of *P*, *N* or *T* axes overlapped (see Fig. 7). The ambiguity of unreliable moment tensors also projected into standard deviations of the DC and non-DC components, which were on average twice larger than those for reliable moment tensors (see Table 2b).

Note that the stability analysis revealed that amplitudes from at least 7 stations were necessary to retrieve reliable moment

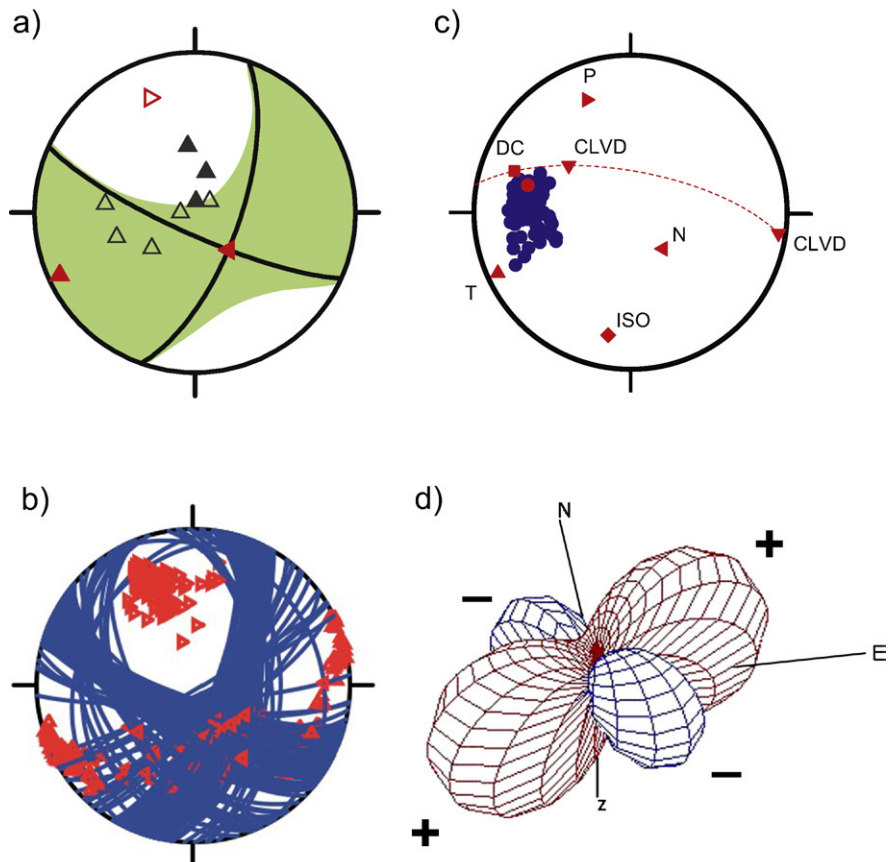


Fig. 6. An example of an unreliably determined mechanism (event 282.024 in Table 1b). For details, see the caption of Fig. 5.

Table 2a  
DC and non-DC components: reliable events

No.	Strike [°]	Dip [°]	Rake [°]	DC [%]	ISO [%]	CLVD [%]	$\sigma^{\text{DC}}$ [%]	$\sigma^{\text{ISO}}$ [%]	$\sigma^{\text{CLVD}}$ [%]	$\sigma^{\text{SUM}}$ [%]
1	288	78	-169	31.7	17.3	-51.1	10.35	5.15	12.93	28.43
2	115	85	-168	79.6	6.5	13.9	11.03	3.63	9.75	24.41
3	118	74	-151	29.8	-10.8	-59.4	15.03	4.43	11.28	30.74
4	104	82	-153	66.8	14.3	-18.9	11.98	10.75	18.22	40.95
5	284	82	147	97.3	1.5	1.2	7.43	3.76	8.97	20.16
6	280	86	174	71.4	-10.9	-17.7	9.37	3.67	9.21	22.25
7	102	80	-157	67.3	28.0	-4.7	10.53	7.18	17.23	34.94
8	108	38	167	39.0	-0.3	-60.7	19.42	7.80	21.90	49.12
9	97	75	-149	39.3	30.9	29.7	11.53	4.06	14.82	30.41
10	107	87	-168	92.7	3.8	-3.6	6.68	4.50	7.56	18.74
11	276	76	149	79.9	-5.4	-14.7	9.81	6.75	12.28	28.84
12	99	69	-141	54.6	33.0	12.4	11.12	4.08	14.72	29.92
13	279	87	-164	28.7	-41.5	29.9	4.70	6.62	6.49	17.81
14	110	69	-169	98.4	0.0	-1.6	6.94	3.63	7.41	17.98
15	121	65	-152	48.1	9.9	42.0	12.13	4.52	9.47	26.12
16	301	66	-104	68.2	25.7	-6.1	9.91	2.84	10.85	23.60
17	112	76	-160	94.3	5.5	0.2	3.78	2.61	5.50	11.89
18	110	61	-179	66.3	-6.3	-27.4	13.60	5.05	10.79	29.44
19	110	70	-162	73.1	-6.5	-20.4	8.76	3.36	6.54	18.66
20	279	68	155	47.1	-14.7	38.2	11.13	5.05	13.40	29.58
21	276	81	153	55.3	-9.1	-35.6	8.81	3.20	11.27	23.28
22	86	71	148	35.8	-26.6	-37.6	9.00	3.21	10.01	22.22
23	281	70	-137	47.5	31.5	-21.0	10.40	7.74	9.97	28.11
24	94	86	138	57.2	0.9	-41.9	18.47	10.30	20.52	49.29
25	291	83	140	53.2	7.8	39.0	10.71	4.24	8.69	23.64
26	254	63	164	63.7	-14.0	22.3	9.19	5.04	12.38	26.61
27	90	84	-163	23.4	-27.3	49.3	13.12	6.74	14.26	34.12
28	110	79	-158	74.8	-6.9	18.3	6.41	3.41	10.62	20.44
29	282	87	157	94.8	2.1	3.1	10.65	5.27	11.92	27.84
30	99	89	-164	62.5	5.8	31.7	13.53	4.90	10.85	29.28
31	285	74	-145	43.8	9.2	47.0	18.53	6.29	15.25	40.07
32	140	85	-139	87.3	7.4	-5.3	4.40	1.72	4.81	10.93
33	293	89	168	79.1	14.2	-6.7	9.01	2.38	10.20	21.59
34	262	52	154	70.3	-22.9	-6.8	5.22	11.66	16.28	33.16
35	105	56	177	43.0	-2.3	-54.6	9.62	3.97	9.50	23.09
36	292	90	150	42.2	22.0	-35.8	14.31	5.54	12.27	32.12
37	275	87	-180	26.7	-15.9	-57.4	17.34	8.22	18.77	44.33
Mean	-	-	-	60.4	1.51	-5.70	10.65	5.22	11.81	27.68

The percentages of the DC, ISO, and CLVD were computed using equations (15–17) of Vavryčuk (2005). The quantities  $\sigma^{\text{DC}}$ ,  $\sigma^{\text{ISO}}$ , and  $\sigma^{\text{CLVD}}$  are the standard deviations of the DC, ISO and CLVD percentages,  $\sigma^{\text{SUM}}$  is defined as  $\sigma^{\text{SUM}} = \sigma^{\text{DC}} + \sigma^{\text{ISO}} + \sigma^{\text{CLVD}}$ .

Table 2b  
DC and non-DC components: unreliable events

No.	Strike [°]	Dip [°]	Rake [°]	DC [%]	ISO [%]	CLVD [%]	$\sigma^{\text{DC}}$ [%]	$\sigma^{\text{ISO}}$ [%]	$\sigma^{\text{CLVD}}$ [%]	$\sigma^{\text{SUM}}$ [%]
38	350	83	-41	34.9	27.3	-37.8	11.26	8.57	15.48	35.31
39	102	59	-148	33.3	12.9	53.8	9.00	4.04	11.88	24.92
40	142	12	-142	31.5	-55.0	-13.5	6.16	6.29	10.65	23.10
41	142	64	-111	80.6	16.2	3.2	19.81	6.97	19.19	45.97
42	92	61	-143	48.3	1.2	-50.5	13.48	10.04	23.94	47.46
43	110	46	-164	33.4	27.4	-39.2	27.33	12.99	34.26	74.58
44	298	12	-108	84.6	-12.7	2.7	23.75	7.46	34.35	65.56
45	201	90	-29	70.3	13.7	-16.0	18.35	12.92	27.82	59.09
46	114	79	-157	62.4	11.0	-26.6	17.61	9.56	17.88	45.05
47	82	56	179	90.8	-5.5	-3.7	24.57	11.53	46.18	82.28
48	241	18	20	42.7	29.3	-28.0	20.43	9.26	20.50	50.19
49	256	70	-161	59.5	4.3	36.2	12.98	7.90	14.94	35.82
50	63	52	13	55.3	-1.4	43.3	18.35	12.92	27.82	59.09
51	285	79	162	69.1	-6.0	24.9	16.52	10.75	26.16	53.43
52	350	28	77	7.6	45.7	-46.7	13.58	4.82	12.21	30.61
Mean	-	-	-	53.62	7.23	-6.53	16.88	9.07	22.88	48.83

For the meaning of quantities, see the legend of Table 2a.

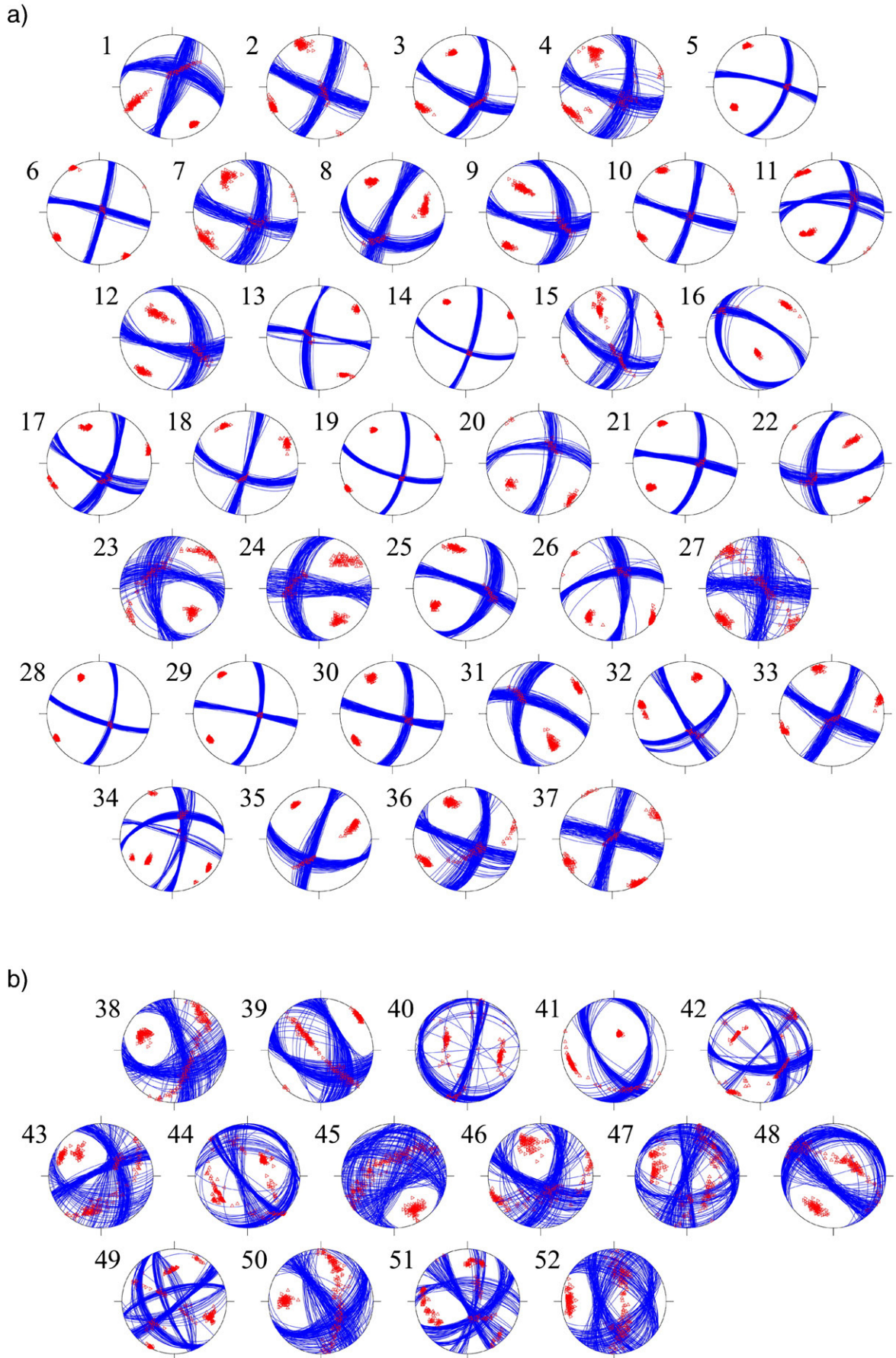


Fig. 7. Distributions of the nodal lines obtained by the inversion of noisy data for 37 reliable (a) and 15 unreliable (b) mechanisms.

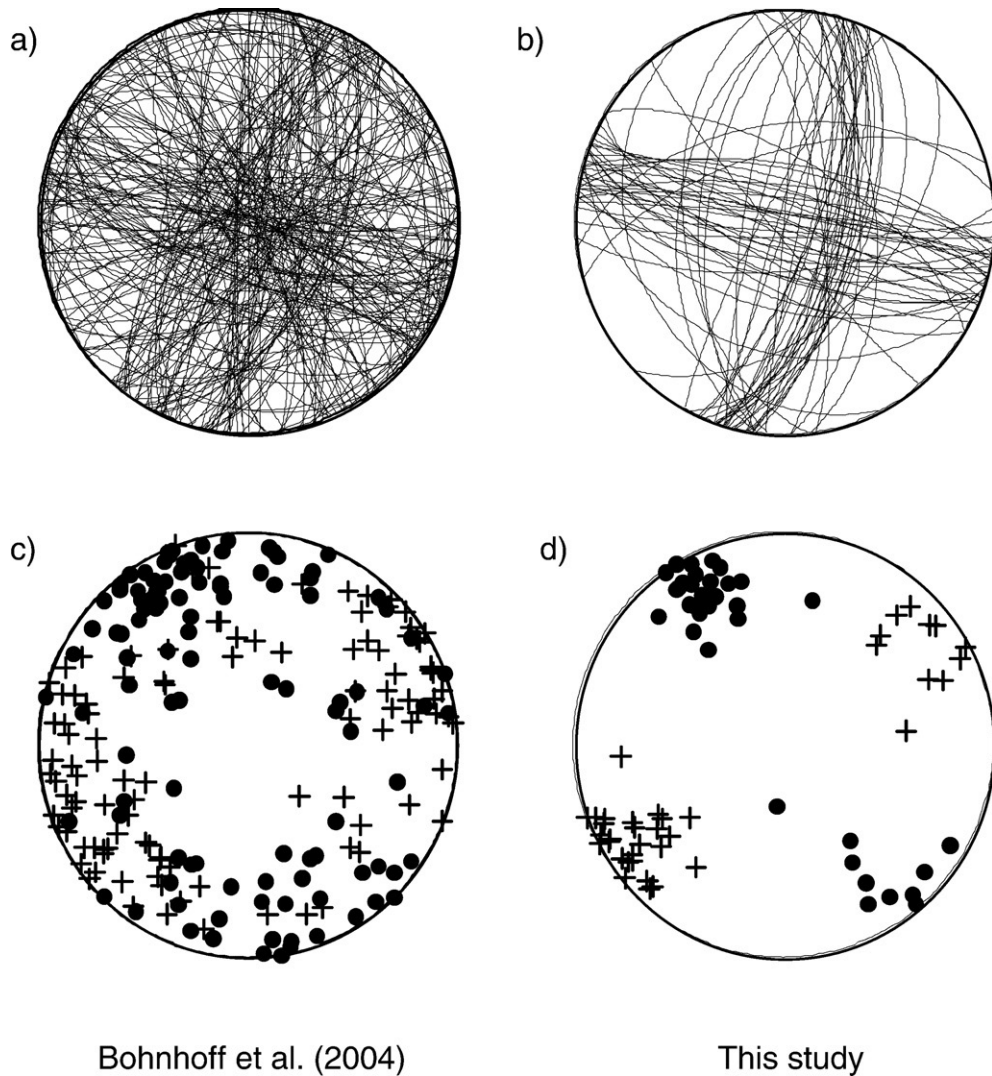


Fig. 8. A comparison of mechanisms of 125 events of Bohnhoff et al. (2004) and those of 37 selected events under study. Nodal lines of 125 (a) and 37 (b) events,  $P/T$  axes of 125 (c) and 37 (d) events. The  $P$  axes are marked by dots, the  $T$  axes by plus signs. Lower-hemisphere equal-area projection is used.

tensors (see Table 1a). Hence the original constraint to analyze events recorded at least at 4 stations was insufficient.

#### 4. Focal mechanisms and tectonic stress

Fig. 8 shows 37 fault plane solutions calculated from reliable moment tensors together with 125 fault plane solutions reported by Bohnhoff et al. (2004). The fault plane solutions of the 37 events under study (see Fig. 8b,d) display preferred strike-slip mechanisms with small normal or reverse components. The  $P$  and  $T$  axes are well clustered having a predominant azimuth in the range of  $N320^{\circ}$ – $340^{\circ}$ E and  $N230^{\circ}$ – $250^{\circ}$ E, respectively. The fault plane solutions of the 125 events of Bohnhoff et al. (2004) (see Fig. 8a,c) are significantly more scattered, but the predominant orientation of the fault plane solutions is similar. The high scatter in the 125 fault plane solutions is probably caused by including events from different depth levels, events with a lower signal-to-noise ratio, and a higher number of weak events. The weak events have, in general, less consistent fault plane solutions reflecting local inhomogeneities of tectonic

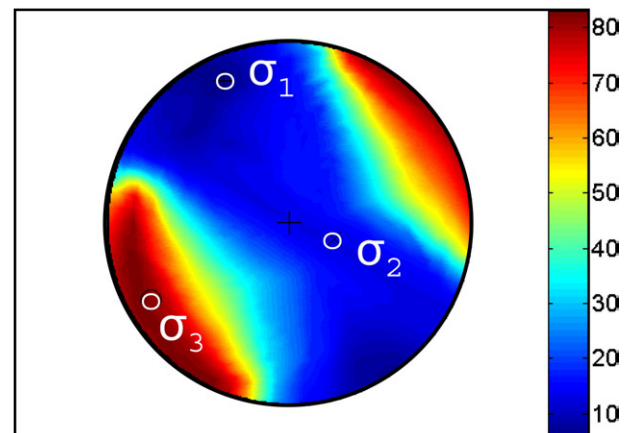


Fig. 9. Inversion for stress. The plot shows the misfit function for stress axis  $\sigma_1$ . The misfit function is defined as the average deviation (in degrees) of the predicted shear traction directions from the observed slips at the faults. Lower-hemisphere equal-area projection is used. The optimum directions of the principal stresses are marked by circles.

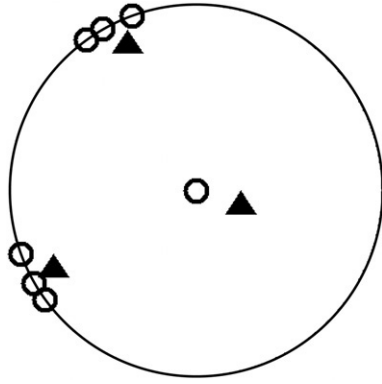


Fig. 10. A comparison of principal stress directions obtained in this paper (full triangles) with those published by other authors (open circles). For values of stress directions and for references, see Table 3.

stress. Moreover, the mechanisms of Bohnhoff et al. (2004) were calculated using the FOCMEC program (Snoke, 2003), which is designed just for retrieving pure DC mechanisms. Since the moment tensors contain significant non-DC components, as discussed further below, the simplistic inversion might also be responsible for the scatter in the deduced focal mechanisms.

The 37 focal mechanisms were inverted for tectonic stress by applying the Gephart and Forsyth inversion method (Gephart and Forsyth, 1984; Michael, 1987; Gephart, 1990; Lund and Slunga, 1999). This method assumes that (1) the stress is uniform in the region, (2) the earthquakes occur on existing faults with varying orientations, and (3) the slip vector points in the direction of the resolved shear traction on the fault. The stress tensor is sought by minimizing the sum of deviations between the shear traction directions and the observed slips at the faults. The misfit function is minimized by using the grid search inversion scheme. The maximum compression  $\sigma_1$  is normalized to be  $-1$ , and the trace of the stress tensor is assumed to be zero,  $\sigma_1 + \sigma_2 + \sigma_3 = 0$ . The inversion yields three angles defining the directions of the three principal stress axes, and shape ratio  $R$ ,  $R = (\sigma_1 - \sigma_2) / (\sigma_1 - \sigma_3)$ .

The inversion for the optimum stress was performed using a  $5^\circ$  grid in seeking the principal stress directions, and a  $0.01$  increment in seeking  $\sigma_2$ . The optimum principal stress directions are (azimuth/plunge):  $\sigma_1 = 335^\circ/15^\circ$ ,  $\sigma_2 = 110^\circ/70^\circ$ ,  $\sigma_3 = 240^\circ/15^\circ$  and the shape ratio is  $0.55$  (Fig. 9). The errors in the plunge and azimuth are estimated to be about  $10^\circ$ . The average deviation angle between the predicted shear tractions and observed slips is  $6.0^\circ$ .

The resolved stress is consistent with the results of Müller et al. (1992), Plenefisch and Bonjer (1997), and Brudy et al.

(1997) obtained for western and central Europe from various types of data, for northern Rhine Graben from focal mechanisms, and for the KTB site from breakouts, respectively (see Fig. 10, Table 3). The stress orientation at the KTB has also been estimated by Bohnhoff et al. (2004), who obtained stress directions rotated by about  $20^\circ$  clockwise compared to our results. This bias might be scaling-related as we considered only the 37 predominantly largest events whereas Bohnhoff et al. (2004) discuss stress field heterogeneity based on 125 focal mechanisms. Besides, also the different level of similar focal mechanisms inverted for the stress tensor might play a role for the results obtained.

## 5. Non-DC components

### 5.1. Amount of the non-DC components

The retrieved moment tensors contain significant non-DC components (see Table 2a). The DC is on average 60% and the non-DC is 40% (the percentages are calculated using Eqs. (15)–(17) of Vavryčuk, 2005). The non-DC components contain both the isotropic (ISO) and the compensated linear vector dipole (CLVD) components, which take positive as well as negative values. Fig. 11 shows an example of an event with positive ISO and CLVD, Fig. 12 shows an event with negative ISO and CLVD. The radiation functions of both events remarkably deviate from the standard quadrefoil form known for DC mechanisms. On average, the CLVD is more pronounced than the ISO: the mean absolute value is 26.1% for the CLVD, but only 13.5% for the ISO. Also the distribution of the CLVD values is different from that of ISO (see Fig. 13). While the distribution of the ISO values is nearly symmetric with a mean value of 1.5%, the CLVD values tend to be more negative, and the mean value is  $-5.7\%$ . Hence, the compressive components slightly prevail over tensile components. Interestingly, the ISO and CLVD differ not only in their distributions, but they also are uncorrelated (see Fig. 14a). The correlation coefficient is only 0.0096 and it does not significantly change when correlating more reliable moment tensors (see Fig. 14b). This is an indication of no trade off between the ISO and CLVD introduced by the moment tensor inversion.

### 5.2. Possible causes of the non-DC components

The non-DC components may be of several possible origins:

- (1) They can be spurious being an artefact of an inaccurate moment tensor inversion due to data limitations and

Table 3  
Stress axes and shape ratio at the KTB site and in the adjacent areas

Reference	Site	$\sigma_1$ (azimuth/plunge)	$\sigma_2$ (azimuth/plunge)	$\sigma_3$ (azimuth/plunge)	$R$
This paper	KTB	$335^\circ/15^\circ$	$110^\circ/70^\circ$	$240^\circ/15^\circ$	0.55
Brudy et al. (1997)	KTB	$340^\circ/0^\circ$	Vertical	$250^\circ/0^\circ$	0.72
Plenefisch and Bonjer (1997)	Rhine Graben	$330^\circ/0^\circ$	Vertical	$240^\circ/0^\circ$	0.5
Müller et al. (1992)	Western Europe	$324^\circ/0^\circ$	Vertical	$234^\circ/0^\circ$	–

The azimuth is measured clockwise from North; the plunge is measured downwards from the horizontal direction.

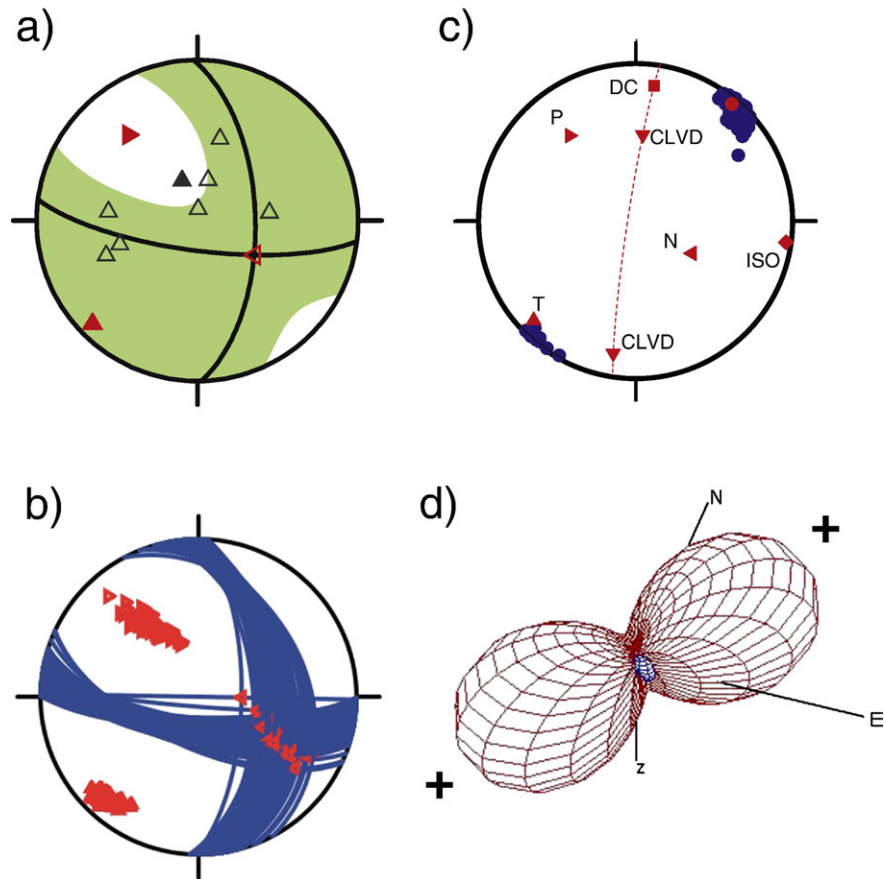


Fig. 11. An example of an extensive mechanism with positive ISO and CLVD components (event 259.065 in Table 1a). For details, see the caption of Fig. 5.

erroneous location of the source. To estimate the errors of the moment tensor inversion, we tested its stability and sensitivity to noise in the data and evaluated the standard deviations of the results (see Table 2a). The mean standard deviations of the DC and non-DC components are estimated to be 10.7% for the DC, 11.8% for the CLVD, and 5.2% for ISO. Although these values are high, it is clear that the presence of the non-DC components cannot be fully explained by the inaccuracy of the moment tensor inversion.

- (2) The non-DC components may originate in shear faulting on a non-planar fault or on a fault composed of several differently oriented subfaults (Sipkin, 1986; Frohlich, 1994). Such mechanisms, however, can never contain an ISO component, because no combination of DC moment tensors, produced by individual sub-events, can generate a non-zero ISO (Julian et al., 1998). Since the ISO is significant in the studied dataset and it is not reasonable to assume that the majority of microearthquakes displayed a complicated faulting geometry, we conclude that this origin is not responsible for the majority of retrieved non-DC components.
- (3) The non-DC components may be produced by tensile faulting owing to high pore pressure. Pore pressure can decrease effective stress on faults and trigger earthquakes. If pore pressure is sufficiently high, it can open the fault

during an earthquake and the resultant mechanism is a combination of shear and tensile faulting (Shimizu et al., 1988; Ross et al., 1996; Julian et al., 1998; Miller et al., 1998; Vavryčuk, 2001, 2002). Such mechanisms should contain both CLVD and ISO components, which must be positive, and their ratio depends on the Poisson ratio at the source (Vavryčuk, 2001). Since the microearthquakes studied are induced by fluid injections into the rock, pore pressure might be anomalous, and the possibility of tensile faulting cannot be excluded. However, the negative mean value of the CLVD and the nearly zero mean value of the ISO indicate that tensile faulting should not be the predominant origin of the non-DC components in the studied dataset. This is supported by no correlation observed between the ISO and CLVD (see Fig. 14). In case of tensile faulting, both non-DC components must correlate: a positive ISO should be associated with a positive CLVD (crack opening) and a negative ISO with a negative CLVD (crack closure).

- (4) One of possible origins of the non-DC components is seismic anisotropy. Anisotropy affects seismic sources and radiated waves in two ways: along a path and at the source. Along a path, anisotropy affects propagating waves by modifying their polarization, velocity and amplitudes. If the path effects of anisotropy are neglected and just isotropic Green functions are used in the moment

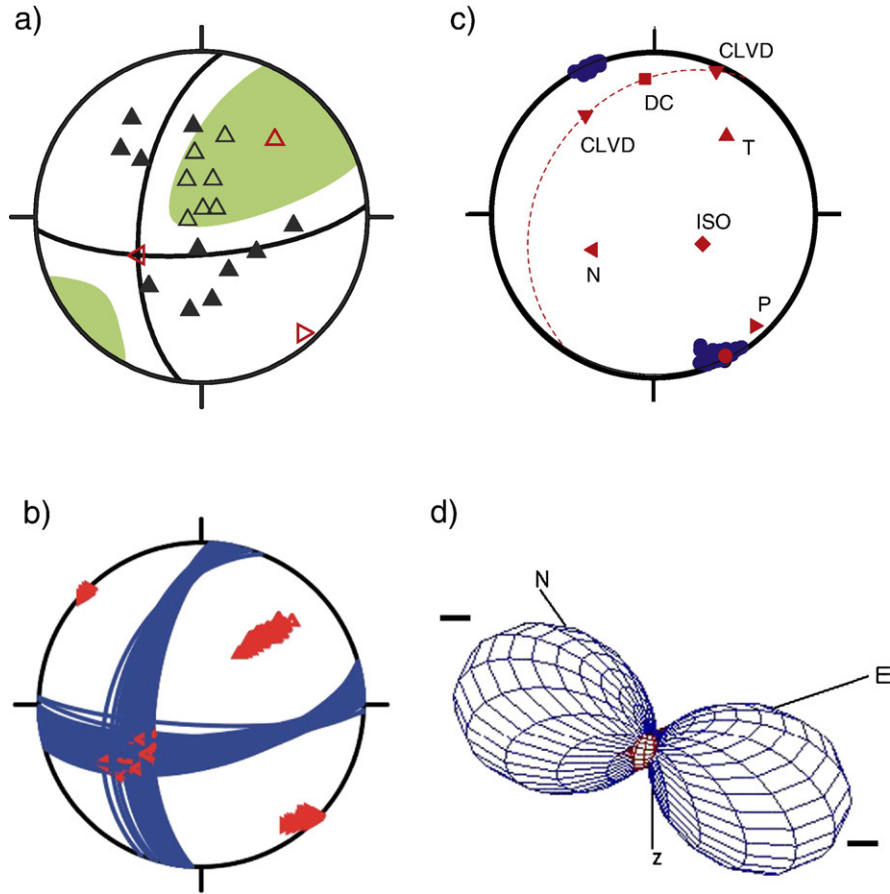


Fig. 12. An example of a compressive mechanism with negative ISO and CLVD components (event 275.094 in Table 1a). For details, see the caption of Fig. 5.

tensor inversion, the inversion can yield spurious non-DC components (Šílený and Vavryčuk, 2000, 2002). The magnitude of these components depends on anisotropy strength, the wave type used in the inversion and on the ray coverage of the focal sphere. The better the ray coverage, the less errors are produced. At the source, anisotropy affects properties of moment tensors and the relation between geometry of faulting and its moment tensor representation. For example, shear faulting in anisotropic focal area is represented by a generally non-DC mechanism (Kawasaki and Tanimoto, 1981; Julian et al., 1998; Rössler et al., 2004; Vavryčuk, 2005, 2006b; Rössler et al., 2007a,b) rather than by a DC mechanism as in isotropic media. The non-DC components depend on symmetry and strength of anisotropy, and on the orientation of faulting with respect to the anisotropy axes. Hence, even in the case of using correct anisotropic Green functions in the moment tensor inversion, shear faulting in anisotropy is associated with non-DC components, which are true and physical. The non-DC components can comprise both the ISO and CLVD and can attain positive as well as negative values. Since several studies confirmed that the rocks in the KTB environment are anisotropic (Rabbel, 1994; Jahns et al., 1996; Okaya et al., 2004; Rabbel et al., 2004) it is very likely that anisotropy is responsible at least for a part of the non-DC components.

## 6. Anisotropy in the focal area

In this section we shall examine the possibility of the non-DC components in moment tensors being produced by anisotropy in the focal area. We shall provide a theoretical background explaining how anisotropy can affect moment tensors and describe a method of determining anisotropy parameters from their non-DC components. Finally, we shall try to extract some information on anisotropy in the focal area from the observed data.

### 6.1. Moment tensors in anisotropic media

The seismic moment tensor  $\mathbf{M}$  in anisotropic media is expressed as (Vavryčuk, 2005, Eq. (4))

$$M_{ij} = c_{ijkl}D_{kl}, \quad (1)$$

where  $c_{ijkl}$  are the elastic parameters of the medium, and  $D_{kl}$  is the source tensor defined as

$$D_{kl} = \frac{uS}{2}(v_k n_l + v_l n_k). \quad (2)$$

Vectors  $\mathbf{v}$  and  $\mathbf{n}$  specify the fault normal and slip direction,  $u$  is the slip and  $S$  is the fault area. If the slip vector lies in the fault plane, the earthquake is shear, if the slip vector is inclined from the fault plane, the earthquake is non-shear (tensile or compressive, see Vavryčuk, 2001).

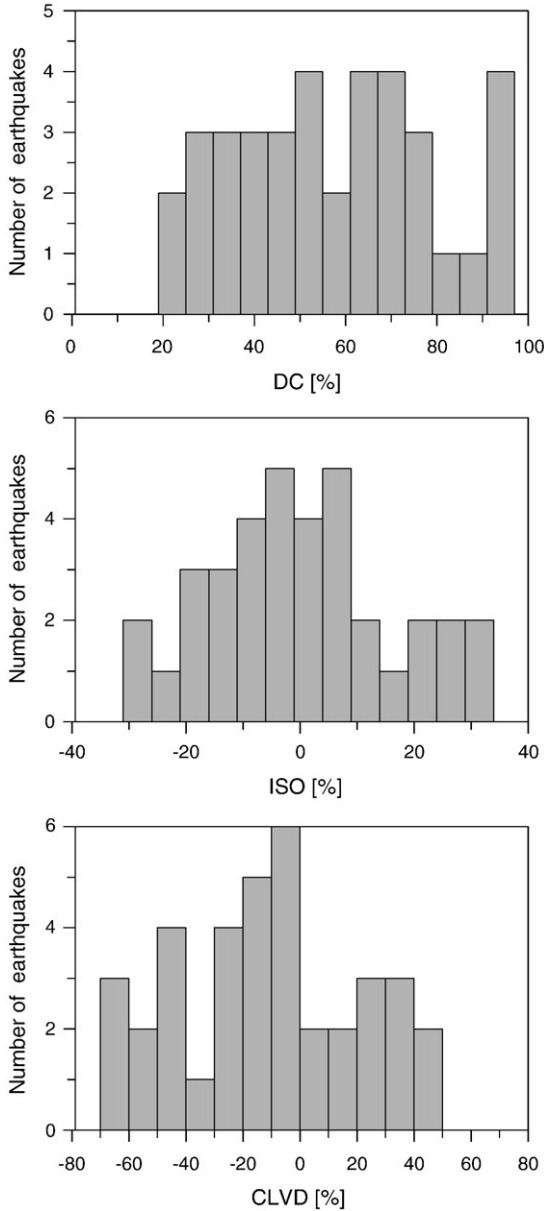


Fig. 13. Histograms of the percentages of the DC and non-DC components. The percentages of the DC, ISO, and CLVD were computed using Eqs. (15)–(17) of Vavryčuk (2005).

Since source tensor  $\mathbf{D}$  is formed by a dyad of vectors  $\boldsymbol{\nu}$  and  $\mathbf{n}$ , it should always have one zero eigenvalue, and subsequently its determinant must be zero:

$$\text{Det}(\mathbf{D}) = 0. \quad (3)$$

If faulting is shear, tensor  $\mathbf{D}$  is constrained to have also zero trace:

$$\text{Trace}(\mathbf{D}) = uS(\mathbf{n} \cdot \boldsymbol{\nu}) = 0, \quad (4)$$

Eqs. (3) and (4) can be used to an advantage in defining the misfit function in the inversion for anisotropy. If we know the moment tensors of many earthquakes that occurred at the same source area, we can invert for elastic parameters  $c_{ijkl}$  minimizing the sum of absolute values of  $\text{Det}(\mathbf{D})$  for all earthquakes. This

can be applied to shear as well as non-shear earthquakes. If we are confident that the studied earthquakes are shear, we can minimize the sum of absolute values of  $\text{Det}(\mathbf{D})$  and  $\text{Trace}(\mathbf{D})$  for all earthquakes. The method can be modified to be applicable also to the inversion from moment tensors, which are constrained to have zero trace (see Vavryčuk, 2004). As expected, if we invert DC moment tensors, the procedure yields an isotropic medium; if we invert the non-DC mechanisms, we can obtain anisotropy.

## 6.2. Inversion algorithm

The extent and quality of a moment tensor data set limit the number of anisotropic parameters which can be inverted for. A general triclinic anisotropy is defined by 21 elastic parameters. However, one of them must always be fixed because of coupling of elastic parameters  $c_{ijkl}$ , slip  $u$  and fault area  $S$ . If we invert from moment tensors of shear earthquakes, another elastic parameter must be fixed because of a special geometry in shear faulting (Vavryčuk, 2004). Hence, one can invert at the most for 20 elastic parameters when using moment tensors of non-shear earthquakes, or for 19 parameters when using moment tensors of shear earthquakes. This requires at least data of 20 non-shear earthquakes, on which we impose condition (3).

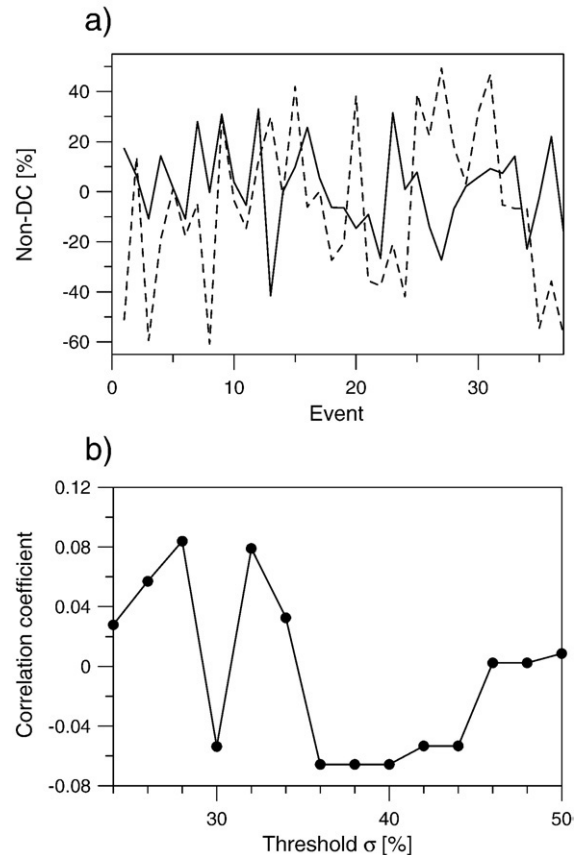


Fig. 14. (a) The CLVD (dashed line) and ISO (solid line) percentages for 37 reliably determined mechanisms (b) The correlation coefficient between the CLVD and ISO components for the moment tensors having  $\sigma^{\text{SUM}}$  (see Table 2a) less than or equal to the threshold value  $\sigma$ . The lower the value of  $\sigma$ , the more confidently moment tensors are used in calculating the correlation coefficient.

Table 4  
Anisotropy models

Anisotropy model	Type	$v_p$ [km/s]	$v_s$ [km/s]	Data	Sample/model identification	Reference
Model I	TI	6.11	3.46	VSP	Model A	Jahns et al. (1996, Table 1)
Model II	TI	5.57	3.33	VSP	Depth: 7.9–8.2 km	Rabbel et al. (2004, Table 1)
Model III	TI	5.82	3.38	Sonic logs	Model B	Jahns et al. (1996, Table 1)
Model IV	ORT	6.27	3.55	Lab	Model C	Jahns et al. (1996, Table 1)

TI — transverse isotropy, ORT — orthorhombic anisotropy,  $v_p$ ,  $v_s$  are average  $P$  and  $S$  velocities.

Each non-shear earthquake thus represents one equation for the anisotropy parameters. If we invert data of shear earthquakes, we need at least 10 moment tensors, on which we impose conditions (3) and (4). In this case, each earthquake represents two equations for the anisotropy parameters. However, because of noise in the data, it is more plausible to invert for anisotropy of higher symmetry to reduce the number of unknowns and to use a much larger number of moment tensors.

Synthetic tests show that an optimum number of accurately determined moment tensors is about 100 when inverting for orthorhombic anisotropy of arbitrary orientation. The moment tensors of non-shear earthquakes can be used, and the misfit function is constructed as the sum of the absolute values of  $\text{Det}(\mathbf{D})$ . Since the number of moment tensors under study is rather small and their accuracy is limited, the inversion for both the elastic parameters and the anisotropy orientation is not possible. Therefore, we must reduce the number of unknowns to stabilize the inversion. This can be done by fixing the elastic parameters and focusing just on finding the optimum orientation of anisotropy. Restricting the inversion to finding only the orientation of anisotropy reduces the number of unknowns either to 3 angles, defining the axes of orthorhombic anisotropy or of anisotropy of lower symmetry, or to 2 angles, defining the symmetry axis of transverse isotropy. Obviously, the restricted inversion can work, provided we know the symmetry of anisotropy and have reasonable estimates of anisotropy in the focal area evaluated in the coordinate system of the anisotropy axes.

### 6.3. Anisotropy at the KTB site

The site of the KTB deep drilling borehole is characterized by a complex and heterogeneous crystalline crust (Emmerrmann

and Lauterjung, 1997). The rock drilled at the KTB basically consists of alternating felsic and mafic layers, mainly biotite gneiss and amphibolite (Rabbel et al., 2004). The layers were steeply folded with dips between  $60^\circ$ – $90^\circ$ , with penetrative foliation between  $50^\circ$ – $80^\circ$ . Field mapping, regional geophysics, and borehole results indicate that the region can be viewed as a block of steeply dipping foliated rocks with a uniform N330°E strike (Berkhemer et al., 1997; Okaya et al., 2004). In such rocks, preferred orientations of minerals prevail, and the crust may display a significant anisotropy. Anisotropy strength might be as high as 10–15% for  $P$  waves, and similar or even higher for  $S$  waves (Babuška and Cara, 1991).

Seismic anisotropy of rocks at the KTB site has been estimated by various authors, using various methods. Rabbel et al. (2004) published elastic parameters of lithologically identical gneiss units at three different depth intervals of the KTB well: 2.2–3.0 km, 7.6–7.9 km, and 7.9–8.2 km. The elastic parameters describe transverse isotropy and were obtained by combining the data of VSP and the dip of rock foliation based on formation micro-scanner logs. Jahns et al. (1994, 1996) reported several sets of elastic parameters of the KTB paragneiss determined using VSP, sonic data and laboratory measurements on a rock sample. The models obtained from the VSP and sonic data are transversely isotropic (TI), the laboratory model is orthorhombic (ORT) having been computed from velocities of  $P$  waves using the approach of Klíma (1973). Jahns et al. (1996) also tried to take into account the effects of in situ water saturation on laboratory measurements, which are usually performed on dry rocks, and proposed two other hypothetical models of the water-saturated KTB paragneiss.

For the purpose of this study, we have employed four anisotropy models, published by Jahns et al. (1996) and Rabbel et al. (2004). The models were obtained from VSP data, sonic logs and from laboratory measurements. Three models are transversely isotropic and one model is orthorhombic (see Table 4). The models predict different directional variations of velocities and also different anisotropy strengths. The  $P$ -wave anisotropy varies between 2–18%, and the  $S$ -wave anisotropy varies between 3–26% (see Table 5). Since the models comprise a fairly high variety of anisotropic behavior (see Figs. 15 and 16), we assume that the true anisotropy is within this variety. In the next, we shall invert for an optimum anisotropy orientation, using all four alternative models, and compare the retrieved orientation with that obtained by other methods.

Table 5  
Anisotropy strength and density-normalized elastic parameters

Anisotropy model	Type	$a^P$ [%]	$a^{SV/S1}$ [%]	$a^{SH/S2}$ [%]	$A_{11}$	$A_{22}$	$A_{33}$	$A_{44}$	$A_{55}$	$A_{66}$	$A_{12}$	$A_{13}$	$A_{23}$
Model I	TI	2.2	4.0	13.8	38.44	38.44	37.21	10.89	10.89	14.36	10.16	14.20	14.20
Model II	TI	17.9	5.5	18.3	37.35	37.35	26.10	9.77	9.77	14.11	9.12	9.15	9.15
Model III	TI	11.6	2.7	26.1	38.18	38.18	30.25	9.69	9.69	16.39	11.40	13.43	13.43
Model IV	ORT	13.6	17.8	8.1	41.27	43.73	33.28	10.14	10.98	15.41	11.09	14.00	14.14

$a^P$ ,  $a^{SV/S1}$ ,  $a^{SH/S2}$  denote the anisotropy strength for  $P$ ,  $SV$  and  $SH$  waves in the case of TI anisotropy and the anisotropy strength for  $P$ ,  $S1$  and  $S2$  waves in the case of ORT anisotropy. The anisotropy strength is defined as  $a = 200(v^{\text{MAX}} - v^{\text{MIN}}) / (v^{\text{MAX}} + v^{\text{MIN}})$ , where  $v^{\text{MAX}}$  and  $v^{\text{MIN}}$  are the maximum and minimum phase velocities of the respective wave. Density-normalized elastic parameters  $A_{kl}$  are in  $\text{km}^2 \text{s}^{-2}$ .

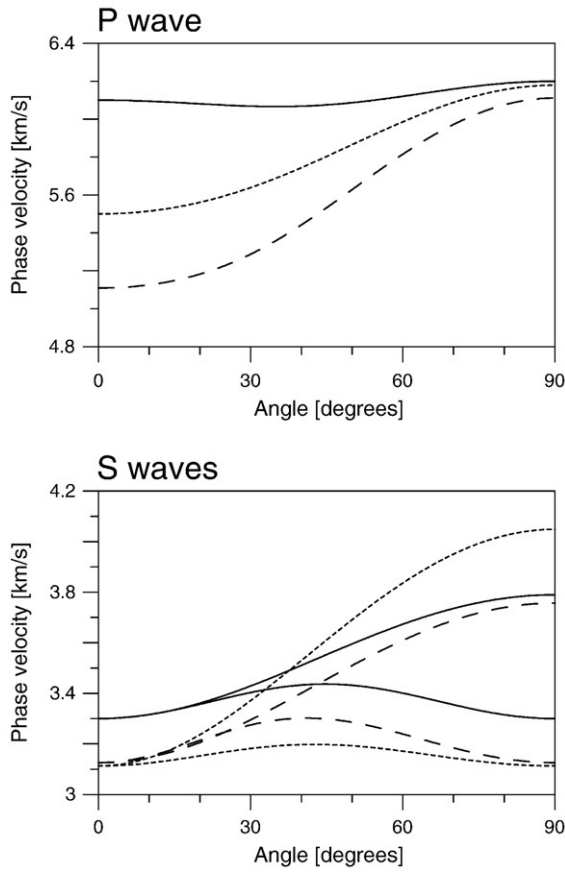


Fig. 15. Directional variations of *P*- and *S*-wave velocities for three transversely isotropic models: Model I (solid line), Model II (dashed line), and Model III (dotted line). For the elastic parameters of the models, see Table 5. The angle presents the deviation between the slowness vector of the wave and the symmetry axis.

#### 6.4. Inversion for optimum orientation of anisotropy from observed data

We adopted four alternative anisotropy models, described in the previous section, and inverted the moment tensors for the optimum orientation of anisotropy. The anisotropy orientation was sought over a sphere in a  $5^\circ$  grid of spherical angles. The misfit function was calculated using Eq. (3) as the sum of determinants of source tensors of all earthquakes under study (see Vavryčuk, 2004, Eq. (10)). Hence, we did not a priori assume any specific type of faulting, and the inversion was applicable not only to shear but also to non-shear earthquakes. At this point the approach is more general than that presented by Vavryčuk (2004, 2006a).

The results of the inversion are summarized in Table 6. Although the anisotropy models used in the inversion were fairly diverse, the found optimum orientations of the anisotropy axes are consistent for all of them. This points to the robustness of the inversion and plausibility of its results. Fig. 17 shows the misfit functions for Models III and IV. Since Model III is transversely isotropic, the inversion yields only the orientation of the symmetry axis. Model IV is orthorhombic, and the inversion yields the orientations of all three anisotropy axes.

The misfit function is normalized so that it equals 1 for an isotropic medium. For some orientations of anisotropy, the misfit function is even higher than for an isotropic medium. The optimum orientation of anisotropy yields the misfit of 0.81 for Model III and 0.77 for Model IV. Hence orthorhombic anisotropy fits the data slightly better than transverse isotropy. Nevertheless, the value of 0.77 of the misfit is still high and points either to discrepancies between the used anisotropy model and the true anisotropy in the focal area, or to the fact that the non-DC components are significantly affected by random

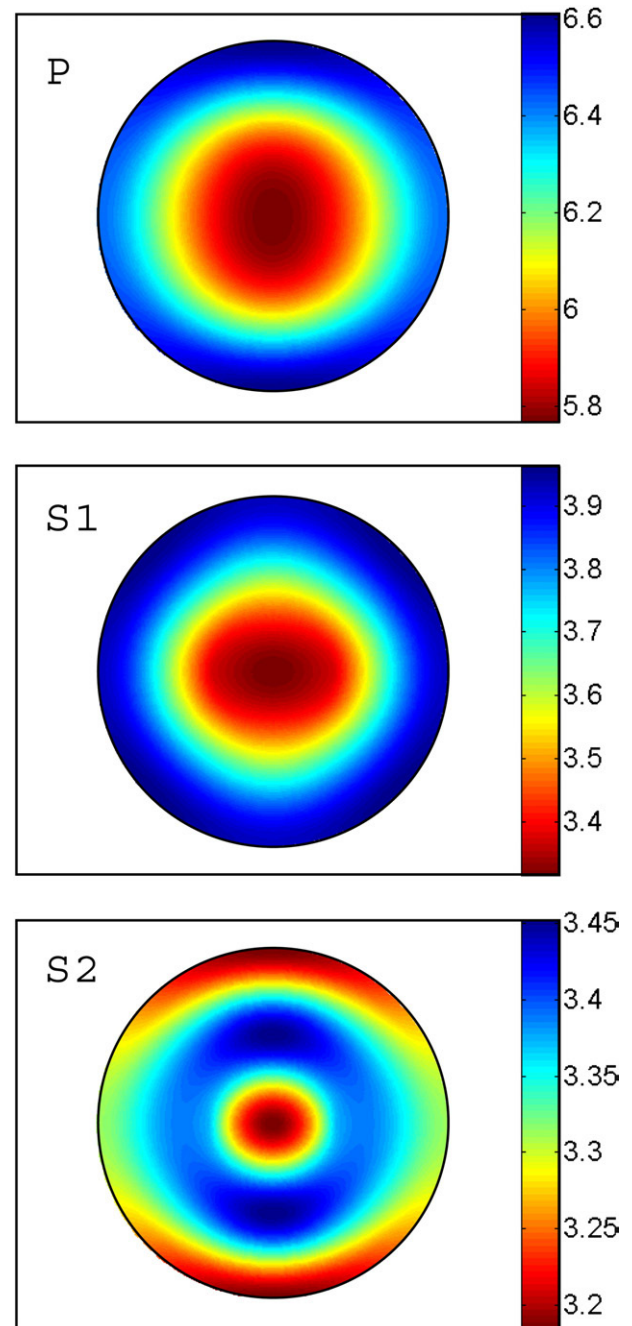


Fig. 16. Directional variations of *P*- and *S*-wave velocities for Model IV displaying orthorhombic anisotropy. Velocities are in km/s. Equal-area projection is used. For the elastic parameters of the model, see Table 5.

Table 6  
Inversion for anisotropy orientation

Model	Type	Axis 1 (azimuth/plunge)	Axis 2 (azimuth/plunge)	Axis 3 (azimuth/plunge)	Misfit
Model I	TI	65°/10°	–	–	0.85
Model II	TI	65°/5°	–	–	0.79
Model III	TI	70°/5°	–	–	0.81
Model IV	ORT	65°/5°	160°/50°	330°/40°	0.77

The misfit is normalized so that it equals 1 for an isotropic medium.

or systematic errors due to limitations of data or erroneous modelling of the structure in the moment tensor inversion.

**7. Non-DC components of the source tensors**

The retrieved orientation of anisotropy can be used to estimate source tensors (2) from moment tensors (1). The source tensors should be, in principle, free of anisotropy effects and should contain only information on geometry of faulting. Similarly as for moment tensors, we can decompose the source tensors into the DC and non-DC components and evaluate their percentages. Fig. 18 shows histograms of the ISO and CLVD components calculated for Model IV. While the distribution of

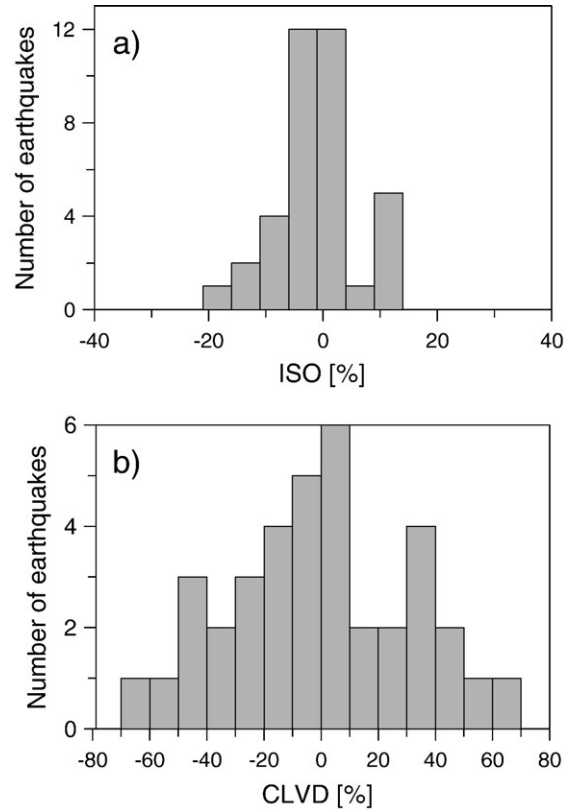


Fig. 18. Histograms of the percentages of the ISO (a) and CLVD (b) components calculated from the source tensors. The source tensors are computed under the assumption of the anisotropic focal area defined by Model IV and oriented by the angles in Table 6.

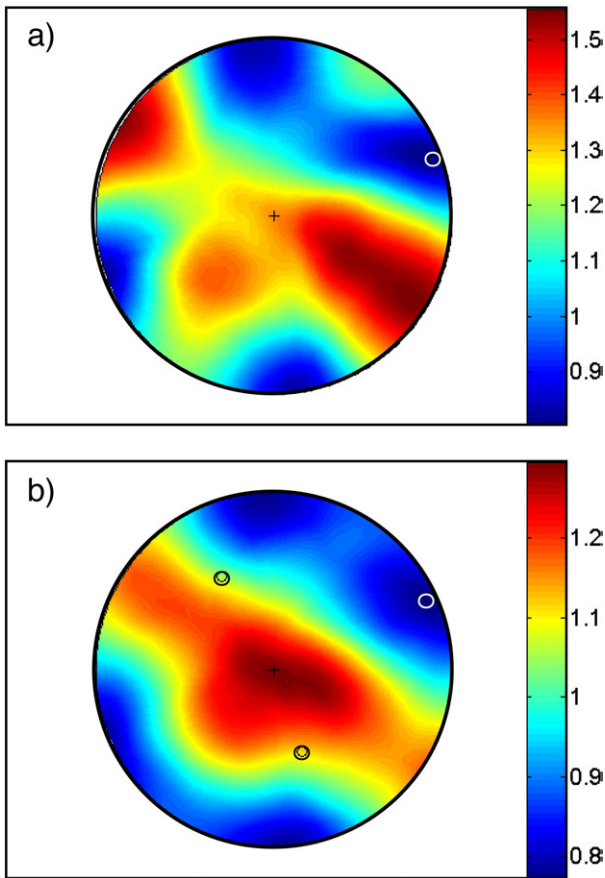


Fig. 17. Inversion for the orientation of Model III (a) and Model IV (b). The misfit function is normalized so that it equals 1 for isotropic medium. For Model IV, the misfit function is displayed for anisotropy axis  $a_3$  (vertical axis in the coordinate system of orthorhombic anisotropy).

the ISO components is very broad for the moment tensors (see Fig. 13), it is remarkably narrow for the source tensors (see Fig. 18). The mean absolute value of the ISO is 13.5% for the moment tensors (see Table 7), but only 5.3% for the source tensors. Also the histograms of the CLVD for the moment and source tensors calculated for Model IV show visible differences (compare Figs. 13 and 18). While the CLVD distribution for the moment tensors is clearly asymmetric, the CLVD distribution for the source tensors is more symmetric. The mean value is shifted from  $-5.7\%$  for moment tensors to  $4.4\%$  for source tensors (see Table 7). Hence, while compressive components slightly prevail over tensile components in the moment tensors, we observe the opposite tendency in the source tensors.

Interestingly, the correlation between the ISO and CLVD components of the source tensors differs from that of the moment tensors. The ISO and CLVD are uncorrelated for moment tensors, but become correlated for the source tensors (Table 7). The correlation further increases when correlating more confident moment tensors, selected as those having standard deviation  $\sigma^{SUM}$  less than a prescribed threshold (see Fig. 19). The maximum value is achieved for Model II, being roughly 0.6. Note that for precise source tensors, the correlation should equal 1. A remarkable correlation between the CLVD and ISO after removing

Table 7  
Non-DC components of the 37 moment and source tensors

Model	Type	$C$	$ISO^{MEAN}[\%]$	$CLVD^{MEAN}[\%]$	$DC^{MEAN}[\%]$	$ ISO ^{MEAN}[\%]$	$ CLVD ^{MEAN}[\%]$	$\Delta ISO$ [%]	$\Delta CLVD$ [%]
—	—	0.028	1.51	−5.70	60.38	13.48	26.14	—	—
Moment tensors									
Source tensors									
Model I	TI	0.438	0.11	0.70	68.97	5.54	25.49	−1.40	6.40
Model II	TI	0.563	2.29	3.42	68.19	6.20	25.61	0.78	9.12
Model III	TI	0.339	0.36	3.80	69.32	5.34	25.35	−1.15	9.50
Model IV	ORT	0.522	1.28	4.38	69.40	5.26	25.33	−0.23	10.08

$C$  is the correlation coefficient between ISO and CLVD for the moment tensors with  $\sigma^{SUM} \leq 24\%$ . Quantities  $ISO^{MEAN}$ ,  $CLVD^{MEAN}$  and  $DC^{MEAN}$  are mean values of percentages ISO, CLVD and DC,  $|ISO|^{MEAN}$ ,  $|CLVD|^{MEAN}$  and  $|DC|^{MEAN}$  are mean values of absolute percentages |ISO|, |CLVD| and |DC| for the whole dataset of 37 events.  $\Delta ISO$  is the difference between the values of  $ISO^{MEAN}$  for source tensors and moment tensors.  $\Delta CLVD$  is the difference between the values of  $CLVD^{MEAN}$  for source tensors and moment tensors.

anisotropy effects provides further evidence of correctness of anisotropy inversion.

## 8. Discussion

Although the quality and extent of the moment tensor dataset did not allow us to invert for a complete elasticity tensor but only for the orientation of anisotropy axes of transverse isotropy or of orthorhombic anisotropy, the results are encouraging. Although we applied four different anisotropy models to mimic

anisotropy in the focal area, the inferred optimum orientation of anisotropy axes is very consistent. The symmetry planes of the TI models and one of the symmetry planes of the ORT model are nearly vertical with a strike of  $N335^\circ\text{--}340^\circ\text{E}$ . This strike coincides well with the strike of  $330^\circ$  typical for many major lithological units and faults (Hirschmann, 1996) and with the azimuth of  $335^\circ\text{--}340^\circ$  of the maximum horizontal compressive stress in the region. It also coincides with the orientation of the TI model inferred from  $P$  waves measured during a moving source profiling experiment (Rabbel et al., 2004; Okaya et al.,

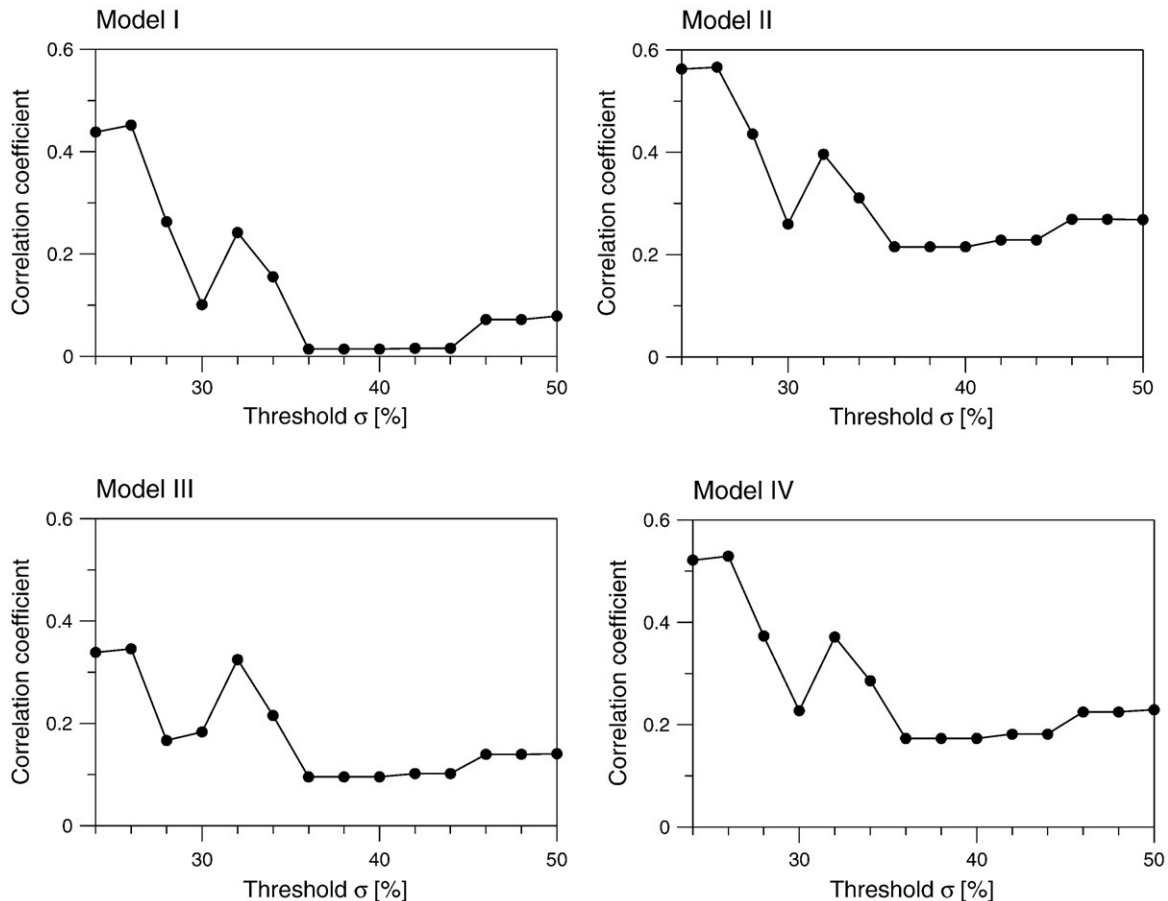


Fig. 19. The correlation coefficient between the ISO and CLVD percentages as a function of threshold deviation  $\sigma$  for Models I–IV. The correlation coefficient is calculated for each value of  $\sigma$  using a family of moment tensors with  $\sigma^{SUM} \leq \sigma$ . The lower the value of  $\sigma$ , the more confidently moment tensors are used for the correlation.

Table 8  
Orientations of anisotropy at the KTB site

Reference	Depth range	Axis 1 (azimuth/plunge)	Axis 2 (azimuth/plunge)	Axis 3 (azimuth/plunge)
This paper	5–6 km	65°/5°	160°/50°	330°/40°
Rabbel et al. (2004, Fig. 12)	0–8 km	244°/13°	139°/48°	345°/39°
Rabbel et al. (2004, Fig. 12)	0–4 km	268°/40°	155°/25°	42°/40°
Rabbel et al. (2004, Fig. 12)	4–8 km	53°/5°	214°/85°	322°/2°

The azimuth is measured clockwise from North; the plunge is measured downwards from the horizontal direction.

2004). Since the ORT model is close to TI, the orientation of the other two axes of the ORT model is more uncertain and less accurately determined. Rabbel et al. (2004, Fig. 12) predicted that their orientation depends on depth and propose three alternative orientations for the depth intervals: 0–4 km, 4–8 km, and an average model for 0–8 km (see Table 8). By comparing our results with these models (see Fig. 20) we obtain the best fit for the average model (0–8 km). In this case all three anisotropy axes coincide almost perfectly with mutual deviations of 18°, 12° and 14°. A worse fit is obtained if our results are compared with the anisotropy model at the 4–8 km depth. Here, both models predict an almost identical symmetry plane, but the two anisotropy axes in this plane deviate from one another by about 40°.

It is also worth mentioning that the non-DC components behave in a more reasonable way if corrected for anisotropy. The ISO percentages were significantly reduced using the anisotropy correction and the mean of the CLVD percentages moved from a negative to a positive value. However, the scatter of the CLVD values remained almost unchanged. This might point to discrepancies between true anisotropy in the focal area and the anisotropy models used in the inversion. It can also indicate that some of the events were generated on irregular or non-planar fractures. Another possibility is that the CLVD components are more vulnerable to errors in the moment tensor inversion than the ISO components.

Since the mean values of the ISO and CLVD components for all events under study are very small, we can conclude that tensile faulting is not a predominant type of faulting for the studied events. If it is present in some of the mechanisms, it must be rather minor. It turns out that pore pressure of the injected fluid did not achieve the minimum compressive stress for the majority of the active fractures, hence the injected fluid triggered only shear events. This is in agreement with the model of fluid-injection-induced seismicity proposed by Baisch and Harjes (2003).

## 9. Conclusions

The fault plane solutions of the 37 selected events with the most reliable moment tensors show preferred strike-slip mechanisms with small normal or reverse components. The predominant azimuth of  $P$  and  $T$  axes is in the range of N320°–340°E and of N230°–250°E, respectively. The optimum principal stress directions inferred from focal mechanisms are (azimuth/plunge):  $\sigma_1=335^\circ/15^\circ$ ,  $\sigma_2=110^\circ/70^\circ$ ,  $\sigma_3=240^\circ/15^\circ$ , and the shape ratio is 0.55. The errors in the plunge and azimuth are

about 10°. The resolved stress is consistent with the results of Brudy et al. (1997) obtained from breakouts.

The retrieved moment tensors contain significant non-DC components. The DC is on average 60% and the non-DC is 40%. The non-DC components contain both the ISO and CLVD components, which attain positive as well as negative values. The ISO and CLVD components are mutually uncorrelated. The mean value of ISO is 1.5%, the mean value of CLVD is –5.7%. The mean value of |ISO| is 13.5% and that of |CLVD| is 26.1%. The non-DC components probably have three major origins: anisotropy in the focal area, errors produced by mismodelling of the medium when calculating the Green functions, and errors produced by the moment tensor inversion due to noise and limitations of input data. The random errors have been suppressed by analyzing only the most reliable moment tensors.

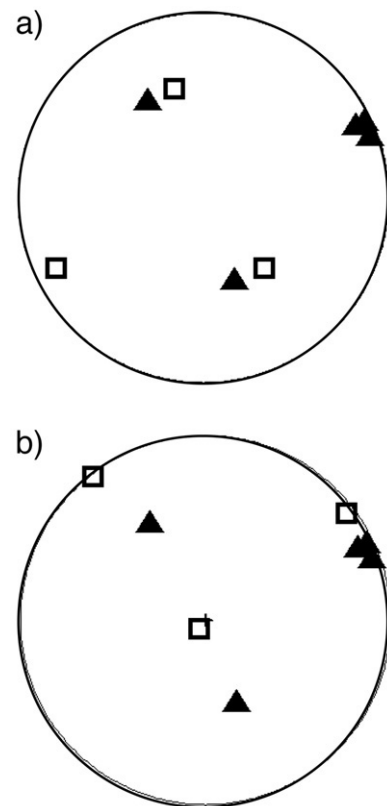


Fig. 20. A comparison of retrieved orientations of anisotropy axes of Models I–IV (full triangles) with the orientations of anisotropy published by other authors (open squares). (a) Model inferred for the depth range of 0–8 km (Rabbel et al., 2004), (b) model inferred for the depth range of 4–8 km (Rabbel et al., 2004). For values of the anisotropy orientations, see Table 8.

The systematic errors have been suppressed by excellent ray coverage of the focal sphere and by focusing on statistical properties of the whole family of moment tensors but not on moment tensors of individual events. Hence, we conclude that the random as well as systematic errors in the moment tensors should not dispute our conclusions about anisotropy.

The optimum orientation of the symmetry plane of TI inferred from non-DC components of the moment tensors is nearly vertical with a strike of N335°–340°E. This strike coincides well with the strike of 330° typical for many major lithological units and faults and with the orientation of the TI model inferred from other seismic experiments (Rabbel et al., 2004; Okaya et al., 2004). After removing the anisotropy effects from the non-DC components, the distribution of the ISO is significantly narrowed. The mean value of the corrected ISO is close to zero and that of the corrected CLVD is shifted from a negative to a positive value. Specifically, assuming ORT anisotropy in the focal area, the mean CLVD is shifted owing to the anisotropy correction by 10% from –5.7% to 4.4%. In accordance with theory, the corrected ISO and CLVD are correlated. The correlation coefficient increases with reliability of non-DC components and attains a value of 0.6 for the most confident moment tensors.

Since the mean values of the corrected ISO and CLVD components are very small, we conclude that shear faulting is a predominant type of faulting in the studied dataset and pore pressure of the injected fluid was not high enough to open existing fractures. This confirms the model of fluid-injection-induced seismicity proposed by Baisch and Harjes (2003).

## Acknowledgements

We thank Gillian R. Foulger and an anonymous reviewer for their reviews, Prof. Wolfgang Rabbel for providing us with details of the anisotropy models at the KTB site and Anthony Lomax for providing us with his program SeisGram2K used for data picking. The work was supported by the Grant Agency of the Academy of Sciences of the Czech Republic, Grants No. KJB300120504, IAA3012309 and IAA300120502, by the Consortium Project SW3D “Seismic waves in complex 3-D structures”, and by the EU Consortium Project IMAGES “Induced microseismics applications from global earthquake studies”, contract No. MTKI-CT-2004-517242. A part of the work was done while the first author was a visiting researcher at the Schlumberger Cambridge Research, Cambridge, U.K.

## References

- Babuška, V., Cara, M., 1991. *Seismic Anisotropy in the Earth*. Kluwer Academic Publishers, London.
- Baisch, S., Bohnhoff, M., Ceranna, L., Tu, Y., Harjes, H.-P., 2002. Probing the crust to 9 km depth: Fluid injection experiments and induced seismicity at the KTB superdeep drilling hole, Germany. *Bull. Seismol. Soc. Am.* 92, 2369–2380.
- Baisch, S., Harjes, H.-P., 2003. A model for fluid-injection-induced seismicity at the KTB, Germany. *Geophys. J. Int.* 152, 160–170.
- Berckhemer, H., Rauen, A., Winter, H., Kern, H., Kontny, A., Lienert, M., Nover, G., Pohl, J., Popp, T., Schult, A., Zinke, J., Soffel, H.C., 1997. Petrophysical properties of the 9-km-deep crustal section at KTB. *J. Geophys. Res.* 102, 18,337–18,361.
- Bohnhoff, M., Baisch, S., Harjes, H.-P., 2004. Fault mechanisms of induced seismicity at the superdeep German Continental Deep Drilling Program (KTB) borehole and their relation to fault structure and stress field. *J. Geophys. Res.* 109, B02309. doi:10.1029/2003JB002528.
- Brudy, M., Zoback, M.D., Fuchs, K., Rummel, F., Baumgärtner, J., 1997. Estimation of the complete stress tensor to 8 km depth in the KTB scientific drill holes: implications for crustal strength. *J. Geophys. Res.* 102 (B8), 18,453–18,475.
- Emmerman, R., Lauterjung, J., 1997. The German Continental Deep Drilling Program KTB: overview and major results. *J. Geophys. Res.* 102, 18,179–18,201.
- Foulger, G.R., Julian, B.R., Hill, D.P., Pitt, A.M., Malin, P.E., Shalev, E., 2004. Non-double-couple microearthquakes at Long Valley Caldera, California, provide evidence for hydraulic fracturing. *J. Volcan. Geotherm. Res.* 132, 45–71. doi:10.1016/s0377-0273(03)00420-7.
- Frohlich, C., 1994. Earthquakes with non-double-couple mechanisms. *Science* 264, 804–809.
- Gephart, J.W., 1990. Stress and the direction of the slip on fault planes. *Tectonics* 9, 845–858.
- Gephart, J.W., Forsyth, D.W., 1984. An improved method for determining the regional stress tensor using earthquake focal mechanism data: application to the San Fernando earthquake sequence. *J. Geophys. Res.* 89 (B11), 9305–9320.
- Hirschmann, G., 1996. KTB — the structure of a Variscan terrane boundary: seismic investigation-drilling-models. *Tectonophysics* 264, 327–339.
- Jahns, E., Rabbel, W., Siegesmund, S., 1996. Quantified seismic anisotropy at different scales: a case study from the KTB crustal segment. *J. Geol. Wiss.* 24, 729–740.
- Jahns, E., Siegesmund, S., Chlupáč, T., 1994. In situ seismic velocities versus laboratory measurements: an example from the KTB. *Sci. Drill.* 4, 215–226.
- Jechumtálová, Z., Šílený, J., 2005. Amplitude ratios for complete moment tensor retrieval. *Geophys. Res. Lett.* 32 art. No. L22303.
- Julian, B.R., Miller, A.D., Foulger, G.R., 1997. Non-double-couple earthquake mechanisms at the Hengill-Grensdalur volcanic complex, southwest Iceland. *Geophys. Res. Lett.* 24, 743–746.
- Julian, B.R., Miller, A.D., Foulger, G.R., 1998. Non-double-couple earthquakes 1: theory. *Rev. Geophys.* 36, 525–549.
- Julian, B.R., Foulger, G.R., 1996. Earthquake mechanisms from linear-programming inversion of seismic-wave amplitude ratios. *Bull. Seismol. Soc. Am.* 86, 972–980.
- Kawasaki, I., Tanimoto, T., 1981. Radiation patterns of body waves due to the seismic dislocation occurring in an anisotropic source medium. *Bull. Seismol. Soc. Am.* 71, 37–50.
- Klíma, K., 1973. The computation of the elastic constants of an anisotropic medium from body waves. *Stud. Geophys. Geod.* 17, 115–122.
- Lund, B., Slunga, R., 1999. Stress tensor inversion using detailed micro-earthquake information and stability constraints: application to Ölfus in southwest Iceland. *J. Geophys. Res.* 104 (B7), 14,947–14,964.
- Michael, A.J., 1987. Use of focal mechanisms to determine stress: a control study. *J. Geophys. Res.* 92 (B1), 357–368.
- Miller, A.D., Foulger, G.R., Julian, B.R., 1998. Non-double-couple earthquakes 2: observations. *Rev. Geophys.* 36, 551–568.
- Müller, B., Zoback, M.L., Fuchs, K., Mastin, L., Gregersen, S., Pavoni, N., Stephansson, O., Ljunggren, C., 1992. Regional patterns of tectonic stress in Europe. *J. Geophys. Res.* 97, 11,783–11,803.
- Okaya, D., Rabbel, W., Beilecke, T., Hasenclever, J., 2004. P wave material anisotropy of tectono-metamorphic terrane: an active source seismic experiment at the KTB super-deep drill hole, southeast Germany. *Geophys. Res. Lett.* 31, L24620. doi:10.1029/2004GL020855.
- Plenefisch, T., Bonjer, K.P., 1997. The stress field in the Rhine Graben area inferred from earthquake focal mechanisms and estimation of frictional parameters. *Tectonophysics* 275, 7–97.
- Rabbel, W., 1994. Seismic anisotropy at the Continental Deep Drilling site (Germany). *Tectonophysics* 232, 329–341.
- Rabbel, W., Beilecke, T., Böhlen, T., Fischer, D., Frank, A., Hasenclever, J., Borm, G., Kück, J., Bram, K., Druivenga, G., Lüschen, E., Gebrande, H., Pujol, J., Smithson, S., 2004. Superdeep vertical seismic profiling at the KTB deep drill hole (Germany): seismic close-up view of a major thrust zone down to 8.5 km depth. *J. Geophys. Res.* 109, B09309.

- Riedesel, M.A., Jordan, T.H., 1989. Display and assessment of seismic moment tensors. *Bull. Seismol. Soc. Am.* 79, 85–100.
- Ross, A.G., Foulger, G.R., Julian, B.R., 1996. Non-double-couple earthquake mechanisms at the Geysers geothermal area, California. *Geophys. Res. Lett.* 23, 877–880.
- Rössler, D., Krüger, F., Rumpker, G., 2007a. Retrieval of moment tensors due to dislocation point sources in anisotropic media using standard techniques. *Geophys. J. Int.* 169, 136–148.
- Rössler, D., Krüger, F., Pšenčík, I., Rumpker, G., 2007b. Retrieval of source parameters of an event of the 2000 West Bohemia earthquake swarm assuming an anisotropic crust. *Stud. Geophys. Geod.* 51, 231–254.
- Rössler, D., Rumpker, G., Krüger, F., 2004. Ambiguous moment tensors and radiation patterns in anisotropic media with applications to the modeling of earthquake mechanisms in W-Bohemia. *Stud. Geophys. Geod.* 48, 233–250.
- Shimizu, H., Matsuwo, N., Ohmi, S., 1988. A non-double-couple seismic source: tensile-shear crack formation in the Unzen Volcanic Region. *Seismol. Res. Lett.* 59 (5), 1988.
- Sipkin, S.A., 1986. Interpretation of non-double-couple earthquake mechanisms derived from moment tensor inversion. *J. Geophys. Res.* 91 (B1), 531–547.
- Šílený, J., Vavryčuk, V., 2000. Approximate retrieval of the point source in anisotropic media: numerical modelling by indirect parametrization of the source. *Geophys. J. Int.* 143, 700–708. doi:10.1046/j.1365-246X.2000.00256.x.
- Šílený, J., Vavryčuk, V., 2002. Can unbiased source be retrieved from anisotropic waveforms by using an isotropic model of the medium? *Tectonophysics* 356, 125–138. doi:10.1016/S0040-1951(02)00380-3.
- Snoke, J.A., 2003. In: Lee, W.H.K., et al. (Ed.), *FOCMEC: Focal mechanism determinations*, in *International Handbook of Earthquake and Engineering Seismology*. Academic, San Diego, California. Chap. 85.12.
- Vavryčuk, V., 2001. Inversion for parameters of tensile earthquakes. *J. Geophys. Res.* 106 (B8), 16.339–16.355. doi:10.1029/2001JB000372.
- Vavryčuk, V., 2002. Non-double-couple earthquakes of January 1997 in West Bohemia, Czech Republic: evidence of tensile faulting. *Geophys. J. Int.* 149, 364–373. doi:10.1046/j.1365-246X.2002.01654.x.
- Vavryčuk, V., 2004. Inversion for anisotropy from non-double-couple components of moment tensors. *J. Geophys. Res.* 109, B07306. doi:10.1029/2003JB002926.
- Vavryčuk, V., 2005. Focal mechanisms in anisotropic media. *Geophys. J. Int.* 161, 334–346. doi:10.1111/j.1365-246X.2005.02585.x.
- Vavryčuk, V., 2006a. Spatially dependent seismic anisotropy in the Tonga subduction zone: a possible contributor to the complexity of deep earthquakes. *Phys. Earth Planet. Inter.* 155, 63–72. doi:10.1016/j.pepi.2005.10.005.
- Vavryčuk, V., 2006b. Focal mechanisms produced by shear faulting in weakly transversely isotropic crustal rocks. *Geophysics* 71, D145–D152. doi:10.1190/1.2236378.
- Wagner, G.A., Coyle, D.A., Duyster, J., Henjes-Kunst, F., Peterek, A., Schröder, B., Stöckhert, B., Wemmer, K., Zulauf, G., Ahrendt, H., Bischoff, R., Hejl, E., Jacobs, J., Menzel, D., Lal, N., VandenHaute, P., Vercoutere, C., Welzel, B., 1997. Post-Variscan and thermal and tectonic evolution of the KTB site and its surroundings. *J. Geophys. Res.* 102, 18,221–18,232.